The Parallel SBAS Approach for Sentinel-1 Interferometric Wide Swath Deformation Time-Series Generation: Algorithm Description and Products Quality Assessment

Michele Manunta, Claudio De Luca, Ivana Zinno, Francesco Casu, Mariarosaria Manzo, Manuela Bonano, Adele Fusco, Antonio Pepe, *Senior Member, IEEE*, Giovanni Onorato, Paolo Berardino, Prospero De Martino, and Riccardo Lanari, *Fellow, IEEE*

***Abstract*— We present an advanced differential synthetic aperture radar (SAR) interferometry (DInSAR) processing chain, based on the Parallel Small BAseline Subset (P-SBAS) technique, for the efficient generation of deformation time series from Sentinel-1 (S-1) interferometric wide (IW) swath SAR data sets. We first discuss an effective solution for the generation of high-quality interferograms, which properly accounts for the peculiarities of the terrain observation with progressive scans (TOPS) acquisition mode used to collect S-1 IW SAR data. These data characteristics are also properly accounted within the developed processing chain, taking full advantage from the burst partitioning. Indeed, such data structure represents a key element in the proposed P-SBAS implementation of the S-1 IW processing chain, whose migration into a cloud computing (CC) environment is also envisaged. An extensive experimental analysis, which allows us to assess the quality of the obtained interferometric products, is presented. To do this, we apply the developed S-1 IW P-SBAS processing chain to the overall archive acquired from descending orbits during the March 2015–April 2017 time span over the whole Italian territory, consisting in 2740 S-1 slices. In particular, the quality of the final results is assessed through a large-scale comparison with the GPS measurements relevant to nearly 500 stations. The mean standard deviation value of the differences between the DInSAR and the GPS time series (projected in the radar line of sight) is less than 0.5 cm, thus confirming the effectiveness of the implemented solution. Finally, a discussion about the performance achieved by migrating the developed processing chain within the Amazon Web Services CC environment is addressed, highlighting that a two-year data set relevant to a standard S-1 IW slice can be reliably processed in about 30 h.The presented results demonstrate the capability of the implemented P-SBAS approach to efficiently and effectively process large S-1 IW data sets relevant to extended portions of the earth surface, paving the way to the systematic generation of advanced DInSAR products to monitor ground displacements at a very wide spatial scale.**

***Index Terms*— Cloud computing (CC), deformation time series, differential synthetic aperture radar interferometry (DInSAR), GPS, Parallel Small BAseline Subset (P-SBAS), Sentinel-1.**

Manuscript received August 28, 2018; revised January 21, 2019; accepted February 25, 2019. Date of publication May 24, 2019; date of current version August 27, 2019. This work was supported by the Italian Civil Protection Department, EPOS-IP, EOSC-hub, ENVRIFAIR, and OpenAIRE-advance projects of the European Union Horizon 2020 for Research and Innovation Program under Grant 676564, Grant 777536, Grant 824068, and Grant 777541, in part by the I-AMICA Project under Grant PONa3_00363, and in part by the IREA-CNR/Italian Ministry of Economic Development DGS-UNMIG Agreement. *(Corresponding author: Michele Manunta.)*

M. Manunta, C. De Luca, I. Zinno, F. Casu, M. Manzo, A. Fusco, A. Pepe, G. Onorato, P. Berardino, and R. Lanari are with CNR-IREA, 80124 Naples, Italy (e-mail: manunta.m@irea.cnr.it; deluca.c@irea.cnr.it; zinno.i@irea.cnr.it; casu.f@irea.cnr.it; manzo.mr@irea.cnr.it; fusco.a@irea.cnr.it; pepe.a@irea.cnr.it; onorato.g@irea.cnr.it; berardino.p@irea.cnr.it; lanari.r@irea.cnr.it).

M. Bonano is with CNR-IMAA, 85050 Potenza, Italy, and also with CNR-IREA, 80124 Naples, Italy (e-mail: manuela.bonano@imaa.cnr.it; bonano.m@irea.cnr.it).

P. De Martino is with Osservatorio Vesuviano, Istituto Nazionale di Geofisica e Vulcanologia, 80124 Naples, Italy, and also with CNR-IREA, 80124 Naples, Italy (e-mail: prospero.demartino@ingv.it).

Digital Object Identifier 10.1109/TGRS.2019.2904912

I. Introduction

DIFFERENTIAL synthetic aperture radar (SAR) interferometry (DInSAR) is a microwave remote sensing methodology playing nowadays a crucial role in the investigation of earth surface deformation phenomena with centimeter to millimeter level accuracy [1], [2]. Indeed, the DInSAR technique permits to measure the deformation component along the radar line of sight (LOS) with a very large spatial coverage capability and with accuracy of a fraction of the wavelength relevant to the transmitted microwave signals [3]. This result is achieved by exploiting the phase difference (interferogram) between pairs of complex SAR images [4]–[7], usually referred to as single look complex (SLC). Moreover, over the last 20 years advanced DInSAR approaches, which allow the retrieval of the temporal evolution of the detected surface deformations by exploiting large multitemporal SAR data sets, have been developed [8]–[17]. Among these, the Small BAseline Subset (SBAS) algorithm [8] computes displacement time series with subcentimeter accuracy [18], [19], by dealing with different spatial scales [14], [20] and multisensor data [21], [22]. As its name suggests, the SBAS approach relies on an appropriate combination of differential interferograms produced by data pairs characterized by small temporal and orbital separation

(baseline) in order to limit the noise (decorrelation) phenomena affecting the interferometric phase signals [23]. We further remark that the SBAS approach has been successfully exploited for the investigation of different scenarios, such as volcanoes, tectonics, landslides, and anthropogenic-induced land motions [24]–[41].

Recently, a parallel version of the SBAS algorithm, referred to as P-SBAS approach [42], which is able to properly exploit distributed computing infrastructures, such as grid and cloud computing (CC) environments, has been developed. It makes use of both multicore and multinode programming techniques, and consists of an *ad hoc* designed distributed-storage implementation, aimed at guaranteeing sustained scalable performances also for massive amounts of data to be processed [43]–[45].

On April 3, 2014, the Sentinel-1A (S-1A) sensor, which is the first of a family of satellites designed to provide C-Band (∼5.5-cm wavelength) SAR data collected in continuity with the first generation ERS-1/2 and ENVISAT SAR missions, was launched by the European Space Agency [46], followed on April 25, 2016 by the launch of Sentinel-1B (S-1B). The S-1 constellation, developed within the European Copernicus Programme, is the fulfillment of the abovementioned DInSAR evolution because, on land, this system is primarily devoted to interferometric applications [47]; moreover, it is intrinsically characterized by small spatial and temporal baselines [48], [49], naturally fitting the SBAS approach rationale. Finally, the Sentinel-1 data are managed according to a free and open access policy, which allows broadening the dissemination and exploitation of the advanced DInSAR methodologies, as for the case of the SBAS approach and of the subsequently developed SBAS-based DInSAR methods and tools [50], [51].

The acquisition mode used over land to generate interferometric wide (IW) swath SAR products is referred to as terrain observation with progressive scans (TOPS) [52]. The TOPS mode has some specific characteristics that must be properly taken into account in order to correctly process the acquired interferometric data. In particular, the already available interferometric processing chains were originally developed to process SAR data acquired with the more conventional stripmap and ScanSAR modes [5] and, accordingly, they require specific algorithmic modifications and enhancements in order to properly generate the S-1 IW products [53]–[59] (e.g., the interferometric SAR data pairs coregistration must guarantee a very high accuracy level, not exceeding 5×10^{-3} samples [60], [61]).

Another key issue to be considered while handling S-1 interferometric SAR data sets is the huge data volume provided by the constellation that, coupled with the large data size of each acquisition (one order of magnitude greater than those collected by the first generation ERS-1/2 C-Band SAR systems), makes the computing efficiency a crucial aspect to be taken into account when dealing with an interferometric S-1 IW processing chain. This is particularly important for the advanced DInSAR processing chains aimed at generating deformation time series, since they may easily involve hundreds of SAR scenes and much more intermediate products for the deformation time series generation [62].

This paper is aimed at describing an advanced DInSAR processing chain based on the P-SBAS algorithm, for the efficient generation of S-1 IW deformation time series. In this framework, an effective solution, which allows the generation of high quality S-1 IW interferograms, is first discussed. Subsequently, we focus on the benefits achievable from the data acquisition characteristics of the IW mode, in terms of parallelization strategy of the developed P-SBAS processing chain; indeed, the available sequence of bursts is considered as a series of separate images to be independently processed. Such a data structure intrinsically drives the parallelization strategy of the S-1 IW P-SBAS processing chain up to the DInSAR interferograms generation step, which can be carried out through the exploitation of efficient algorithms and high-performance distributed computing infrastructures for tackling the available huge data flow.

An extensive quality assessment of the products obtained through the presented P-SBAS processing chain is also carried out. This is based on the investigation of an S-1 IW multitemporal data set relevant to the overall Italian territory and including 2740 SLC IW slices (where a slice represents an area on the ground of about 250×250 km^2) acquired from descending orbits during the March 2015–April 2017 time span. Moreover, for this analysis, we also benefit from the continuous GPS position time series provided by the Istituto Nazionale di Geofisica e Vulcanologia—Osservatorio Vesuviano (INGV-OV) and the Nevada Geodetic Laboratory at the University of Nevada, Reno, USA (UNR-NGL). Finally, a discussion about the performance achieved through the S-1 IW P-SBAS processing chain implemented within the Amazon Web Services (AWS) CC environment [63], in terms of elapsed processing times, is addressed.

This paper is organized as follows. In Section II, the main acquisition characteristics of the S-1 IW mode are briefly summarized. Section III is specifically focused on the technical aspects of the procedures developed for the accurate interferograms generation operations. Section IV describes the implemented S-1 IW P-SBAS processing chain, highlighting the main algorithmic advancements introduced to deal with Sentinel-1 TOPS data and describing the adopted parallelization processing strategy. In Section V, an extended quality assessment of the generated interferometric products is presented, as well as a discussion on the computing performances of the S-1 IW P-SBAS processing chain implemented within the AWS CC environment. Finally, Section VI provides some conclusive remarks.

II. S-1 IW Mode Main Characteristics for DInSAR Analyses

The Sentinel-1 constellation provides an unprecedented operational capability for intensive radar mapping of the earth surface. Indeed, it is designed to guarantee wide area coverage, high revisit frequency (6 days revisit time with S-1A and S-1B fully operative), timeliness and reliability for operational services and applications by exploiting long data

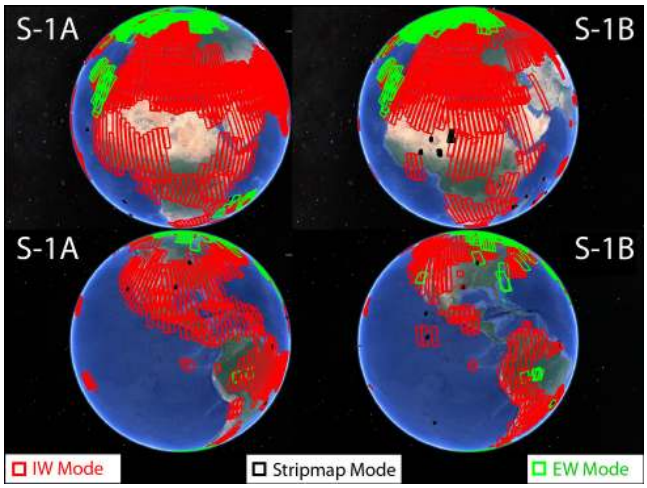

Fig. 1. Example of Sentinel-1A and Sentinel-1B spatial coverage over Europe, Africa, and America. In particular, in this case, we consider the time interval between July 11, 2018 and July 23, 2018. Note that the red areas represent the IW acquisitions, whereas with the green and black colors, we indicate the EW and stripmap ones, respectively, (ESA source).

time series, with a completely free and open access data policy [48].

As an example, we show in Fig. 1 the 2-week spatial coverage of the Sentinel-1 constellation by representing in red, green, and black colors the footprint of the data that are acquired through the IW swath (∼250 km of range swath extension), the extra wide swath (∼400 km of range swath extension) and the stripmap (∼100 km of range swath extension) SAR modes, respectively. Clearly, an outstanding huge amount of data, nowadays approximately 12 TB per day (Fig. 2), is provided and therefore one of the main issues to face is related to the management of such a big data volume, in terms of both quantity of data to store and data size to deal with. Moreover, the development of processing chains, able to automatically and efficiently process large Sentinel-1 data sets, is strongly envisaged. In this context, in order to optimize both the storage and the processing of S-1 IW data, the exploitation of distributed computing architectures, such as grid and CC infrastructures, is foreseen because they have already shown to provide an excellent solution to access extensive collections of storage and computing resources [43], [44], [64].

In the following, we focus on the S-1 IW mode that is extensively exploited for imaging land areas where the investigation of surface deformation phenomena, through DInSAR analyses, represents a high priority (Fig. 1). For what concerns the IW SAR mode we remark that, in order to achieve its wide range footprint of about 250 km, the radar scenes are collected by exploiting the already referred TOPS acquisition mode [52] that is somehow similar to the ScanSAR one [65]. Indeed, during the acquisition time the antenna beam is cyclically switched along the range direction among different swaths, thus allowing a significant improvement of the range coverage; however, unlike the ScanSAR mode, the TOPS one scans the image with significantly longer bursts obtained through the rotation (steering), along the azimuth direction, of the antenna beam from backward to forward (Fig. 3).

The S-1 IW SAR data were already successfully exploited in different DInSAR applications [66]–[69]. These DInSAR results can be achieved because a high level of temporal synchronization is guaranteed for the bursts (corresponding to the same area on the ground) of the multitemporal S-1A and S-1B SAR acquisitions, thus allowing us to preserve the interferometric coherence [6]. However, an effective DInSAR processing of the S-1 IW data requires the development of appropriate algorithms to properly extract accurate information from these data. In particular, since each S-1 IW burst is characterized by large along-track Doppler centroid variations of about 5000 Hz, if misregistration errors greater than a few thousandths of sample are present between the interferometric burst pairs, undesired azimuthal phase ramps in the interferometric phase signals will definitely occur. As a consequence, in order to avoid the presence of these unwanted phase contributions, procedures performing the coregistration step with a very high accuracy level, that is, guaranteeing errors smaller than 0.005 samples [61] must be implemented.

Another key element to be considered in the development of an S-1 IW interferometric processing chain is the constellation "orbital tube." This is very short, having a nominal diameter of about 200 m for what concerns the baseline component perpendicular to the radar LOS, referred to as perpendicular baseline, which is much smaller than the interferometric critical baseline value [5].

To pictorially represent the achieved short orbital tube for the S-1 constellation, we compare in Fig. 4 the spatial baseline distributions in the temporal/perpendicular baseline plane for the ASAR-ENVISAT and the Sentinel-1 sensors, by considering a sample data set acquired over the Naples bay test area. The achieved reduction of the baseline tube is evident for the S-1 acquisitions: the standard deviation value of the perpendicular baselines goes from 360 m of the ASAR-ENVISAT data set to 50 m of the S-1 one (dashed black and red lines in Fig. 4, respectively). Such a feature, which allows to drastically minimize the decorrelation noise affecting the generated interferograms, makes the Sentinel-1 constellation an intrinsically small baseline (SB) system and the data particularly suitable to be processed through advanced DInSAR techniques like the SBAS one [8].

These peculiarities have been properly taken into account to develop the interferometric processing chain for the generation of deformation time series from S-1 IW multitemporal data, which is presented in the following.

III. S-1 IW Burst Interferograms Generation

Let us start our analysis by considering: 1) a set of N SAR images, acquired at the ordered times $\boldsymbol{t} = [t_0, t_1, \ldots, t_{N-1}]$, and 2) a sequence of M interferometric SAR data pairs characterized by short temporal and perpendicular baseline values. We remark that, due to the already discussed large amount of S-1 acquisitions and to the narrowness of the S-1 orbital tube (Fig. 4), even a SB selection may lead to the identification of several thousands of possible interferometric data pairs. For this reason, in order to reduce the computation time without losing relevant information, an additional constraint on the maximum number, say $D_{\max} = 2k_{\max}$,

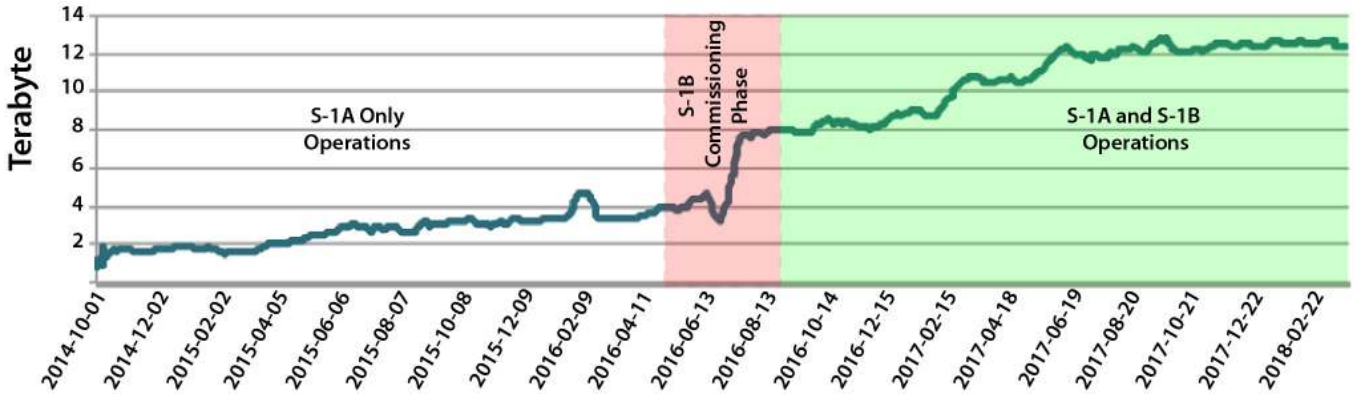

Fig. 2. Sentinel-1 temporal evolution of the average daily production and archiving volumes (ESA source).

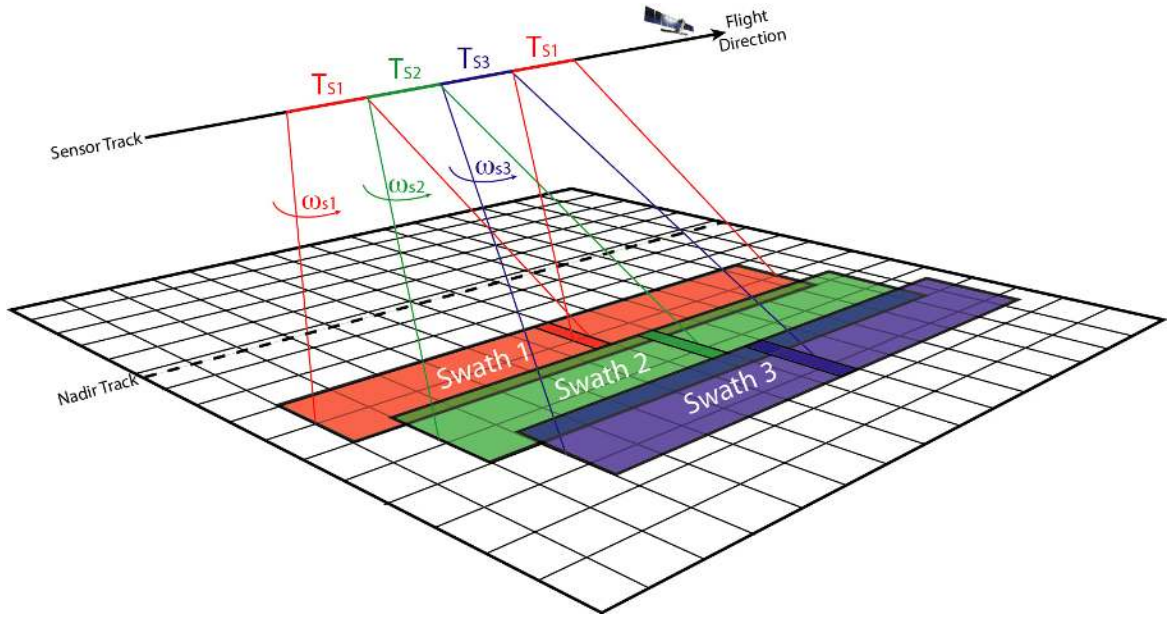

Fig. 3. Schematic representation of the TOPS acquisition mode used to collect the S-1 IW data. Note that similar to ScanSAR mode, the antenna beam is cyclically steered along the range direction to acquire data from different swaths. Moreover, in order to acquire each azimuthal data burst of temporal duration T_S (T_{S1}, T_{S2}, and T_{S3}, depending on the considered swath), the system electronically steers the beam from backward to forward along the azimuth direction with an angular frequency ω_s (ω_{s1}, ω_{s2}, and ω_{s3}, depending on the considered swath).

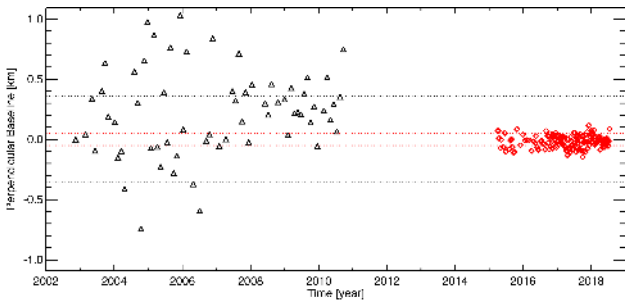

Fig. 4. Comparison between the spatial baseline distributions in the temporal/perpendicular baseline plane for two sample data sets, relevant to the ASAR-ENVISAT (black triangles) and the S-1 (red diamonds) systems, acquired over the Napoli Bay test area. The black and red dashed lines represent the standard deviation values of the spatial baselines computed for the ASAR-ENVISAT and S-1 data sets, respectively.

of DInSAR data pairs involving each SAR image is imposed. In particular, we consider the data pairs relevant to the $k_{\max}$ temporally consecutive acquisitions (whenever available).[1] Accordingly, the total number of generated interferograms is as follows:

$$M = k_{\max} N - \sum_{i=1}^{k_{\max}} i. \tag{1}$$

Note that this interferometric pair selection allows us to avoid to drastically increase the total number of DInSAR data pairs to be processed but, at the same time, permits to preserve the time redundancy of the network of SB interferograms exploited by the P-SBAS processing chain discussed in Section IV.

As previously said, one of the main issues of an S-1 IW DInSAR processing chain is represented by the correct generation of the interferograms; to achieve this task it is widely

[1]Typically, for each SLC scene, we consider the six temporally consecutive acquisitions (whenever available).

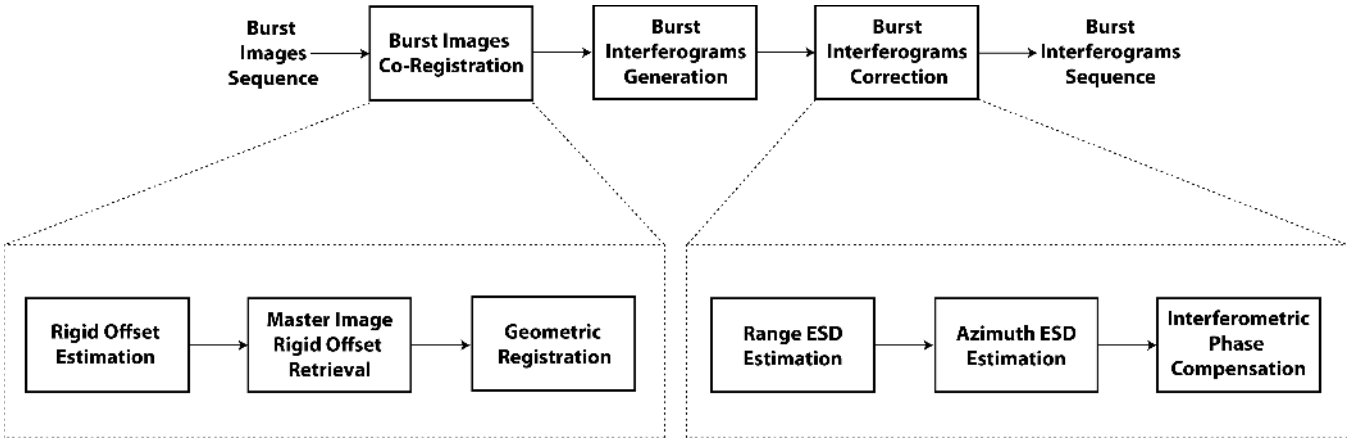

Fig. 5. Block diagram of the implemented interferogram generation procedure. Note that the operations implementing the burst images coregistration and the burst interferogram correction have been further detailed.

recognized that the azimuth coregistration[2] of the SAR images has to be as accurate as possible in order to achieve a maximum error not exceeding 5×10^{-3} samples [61].

In order to reach the goal to properly generate S-1 IW interferograms, we consider the workflow shown in Fig. 5, where the implemented operations are carried out on a burst-by-burst basis. In particular, the interferogram generation operation is accomplished via three operations. Let us start by considering the first one, named burst images coregistration, which is based on the cascade of three steps, referred to as rigid offset estimation, master image rigid offset retrieval, and geometric registration, respectively. The first two steps of this procedure (i.e., the rigid offset estimation and master image rigid offset retrieval) allow us to precisely estimate the rigid shift between each SAR image and a selected reference one, referred to as master image; the achieved results are subsequently used to correctly carry out the geometric registration step based on the approach presented by Sansosti *et al.* [70] that allows us to achieve a temporal sequence of coregistered burst images.

We remark that the rigid offset estimation step exploits the spatial coherence measurements carried out on the selected SB interferometric SAR data pairs and is performed on a single patch, extracted from a chosen burst, characterized by high spatial coherence values [71]. Clearly, in order to maximize the robustness of the rigid offset estimation step, the misregistration errors, namely, $\mathbf{psh} = [\mathrm{psh}_0, \mathrm{psh}_1, \ldots, \mathrm{psh}_{M-1}]$, are evaluated on the selected M (SB) interferometric pairs.

Subsequently, in order to retrieve the master image rigid offset values corresponding to each of the $N-1$ SAR acquisitions, the following system of linear equations is solved:

$$\begin{cases} \mathrm{sh}_0 - \mathrm{sh}_1 = \mathrm{psh}_0 \\ \mathrm{sh}_0 - \mathrm{sh}_2 = \mathrm{psh}_1 \\ \ldots \\ \mathrm{sh}_i - \mathrm{sh}_{i+k} = \mathrm{psh}_j \\ \ldots \\ \mathrm{sh}_{N-2} - \mathrm{sh}_{N-1} = \mathrm{psh}_{M-1} \end{cases} \tag{2}$$

[2]We focus on the azimuth co-registration because in the range direction standard methods, already successfully exploited for the stripmap and ScanSAR modes, can be straightforwardly applied.

where sh_i, $i = 0, \ldots, N-1$, represents the unknown rigid offset of the ith SAR scene, psh_j, $j = 0, \ldots, M-1$ (with $M > N$), is the estimated rigid offset for the jth interferometric pair, and $k = 1, \ldots, k_{\max}$ accounts for the number of data pairs that involve each SAR scene. The system of equations (2) is full rank since it exhibits a number of independent equations equals to the unknowns (the rigid offset relevant to the master image is clearly equal to zero); therefore, the least-squares (LS) solution of (2) is unique and, by considering a matrix notation, it can be easily computed as follows [8]:

$$\mathbf{sh} = \mathbf{A}^{\#} \cdot \mathbf{psh} \text{ with } \mathbf{A}^{\#} = (\mathbf{A}^{\mathrm{T}}\mathbf{A})^{-1}\mathbf{A}^{T} \tag{3}$$

where $\mathbf{sh} = [\mathrm{sh}_0, \ldots, \mathrm{sh}_i, \ldots, \mathrm{sh}_{N-1}]$ represents the LS estimate vector of the rigid offset values corresponding to the SAR images and $\mathbf{A}$ is a $M \times N$ matrix, directly depending on the set of the selected SB interferometric pairs, that assumes the following structure:

$$\mathbf{A} = \begin{bmatrix} 1 & -1 & 0 & 0 & 0 \\ 1 & 0 & -1 & 0 & 0 \\ \ldots & \ldots & \ldots & \ldots & \ldots \\ 0 & 0 & 0 & 1 & -1 \end{bmatrix} \tag{4}$$

where each row represents an interferometric pair, each column a SAR acquisition of the data set, and 1 and -1 are obtained in correspondence to the indexes associated with the master and slave images of the Mth interferometric pair, respectively.

Opposite to directly computing the rigid offset between each SAR image and the master one, this approach benefits, as already said, from the high interferometric coherence values achieved thanks to the exploitation of SB data pairs; moreover, it allows mitigating possible small estimation errors by making use of LS method, and to quantitatively assess the correctness of the achieved solution (3) by evaluating the estimated errors of the obtained results with an accuracy of a few tenths of samples. It is worth noting that the rigid offset estimation procedure, originally presented in [71], is an SBAS-like method; indeed, the algorithm to estimate the misregistration time series from the misregistration errors of the SB pairs is equivalent to the procedure to retrieve the displacement time series from the SB unwrapped interferograms [8]. The same

approach, applied again into the following range and azimuth ESD estimation blocks (Fig. 5), has also been considered in [61] and [72] to strengthen the coregistration procedure.

Following the evaluation of **sh** in (3), each burst of the exploited SAR scenes can be easily registered with respect to the corresponding one of the master image by applying the geometric registration procedure described in [70].

From each coregistered burst images sequence, a set of M SB multilook differential interferograms is then generated. Because this step is performed at the burst granularity level, it can be easily parallelized on several computing nodes to reduce the overall processing time, as discussed in Section IV.

However, as said before, the coherence-based misregistration error estimation procedure has accuracy on the order of few tenths of samples. This is typically accurate enough for SAR data acquired through the conventional stripmap mode but not for the S-1 IW data. Indeed, due to the TOPS-related large Doppler centroid azimuth variations for each IW burst, small residual azimuth misregistration errors introduce significant phase artifacts in the burst interferograms generation [61] that have to be avoided. To do this, let us start by considering that the phase pattern $\phi^{\text{res}}(x,r)$ due to these residual misregistration errors can be expressed, for each SAR pixel of coordinates (x,r), as follows [60]:

$$\phi_j^{\text{res}}(x,r) = 2\pi \times f(x,r) \times \Delta t_j^{\text{res}},$$
$$\text{with}\,\Delta t_j^{\text{res}} = \frac{\text{psh}_j^{\text{res}}}{\text{PRF}}, \quad \forall j = 0,\ldots,M-1 \tag{5}$$

where $f(x,r)$ represents the Doppler centroid values (expressed in Hz) derived from the azimuth antenna steering rate information and computed for each pixel, PRF is the radar pulse repetition frequency, and Δt_j^{res} and $\text{psh}_j^{\text{res}}$ are the residual misregistration errors between the images involved in the jth interferograms, expressed in seconds and samples, respectively. Because $f(x,r)$ changes along the azimuth direction with a linear function and Δt_j^{res} can be considered constant for a slice, the misregistration phase $\phi_j^{\text{res}}(x,r)$ behaves as a phase ramp along the azimuth direction.

An effective way to estimate Δt_j^{res} and to filter out $\phi_j^{\text{res}}(x,r)$ from the interferometric phase signals is based on the application of the enhanced spectral diversity (ESD) method [53] which properly exploits the overlapping areas between consecutive bursts. In this case, the same area is illuminated in the two adjacent bursts with different squint angles and, therefore, with different Doppler centroid values. By exploiting this characteristic and neglecting any other phase component (related, for instance, to different atmospheric path delays or surface displacements that could occur between the acquisition epochs of the two bursts), the residual misregistration error between the SLC scenes involved in the jth interferograms can be expressed as follows [60]:

$$\Delta t_j^{\text{res}} = \frac{\Delta\phi_j^{\text{res}}(x,r)}{2\pi \times \Delta f(x,r)} \tag{6}$$

where $\Delta\phi_j^{\text{res}}(x,r)$ represents the interferometric phase difference between the two consecutive bursts computed in the overlapping region, and $\Delta f(x,r)$ is the difference between the corresponding Doppler centroids.

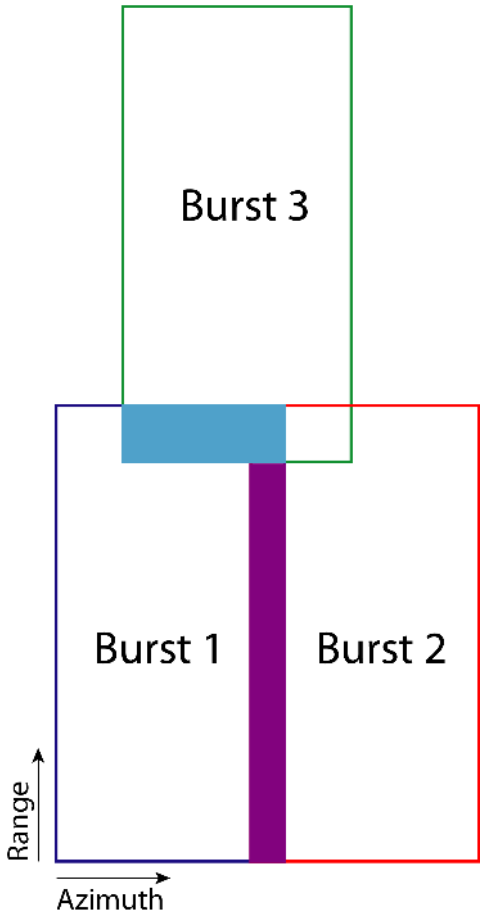

Fig. 6. Schematic representation of the overlapping areas between adjacent bursts in the S-1 system. The light blue and purple colors identify the range and azimuth overlapping zones, respectively.

We remark that although the ESD method represents an efficient and accurate way to estimate residual misregistration errors, its effectiveness can be significantly reduced in presence of large errors. Indeed, the phase term $\Delta\phi_j^{\text{res}}(x,r)$ can be effectively measured only in the wrapped form, i.e., within the $[-\pi,\pi]$ interval. If we consider the typical configuration of the S-1 IW scenes (in the burst overlapped azimuthal area $\Delta f(x,r)$ is approximately equal to 5000 Hz and PRF $= 486.486$ Hz), a 2π residual phase variation corresponds to a misregistration error of about 0.1 samples; therefore, the maximum shift that can be measured through the ESD method corresponds to ± 0.05 samples. This maximum shift value is often too small to correctly estimate the residual misregistration errors following the coregistration operation based on the previously described rigid offset estimation step exploiting the spatial coherence measurements.

In order to overcome this limitation and to correctly estimate the residual misregistration errors, we implement the burst interferogram correction operation as a cascade of three steps referred to as range ESD estimation, azimuth ESD estimation, and interferometric phase compensation, respectively (see Fig. 5). A key element in this case is represented by the exploitation of the ESD method that is applied to different overlapping burst regions. Indeed, as pictorially depicted in Fig. 6, two consecutive bursts are characterized by

two overlapping areas, along the range direction (light blue area in Fig. 6) and along the azimuth one (purple area in Fig. 6), with different $\Delta f(x, r)$ values that can be profitably exploited within the ESD procedure. In particular, concerning the range direction, the pixels located in the overlapped area between bursts 1 and 3 have a Doppler centroid difference of about 1500 Hz, which allows us to estimate, through the ESD method, a maximum misregistration error of about ± 0.15 samples from the wrapped phase signal.

Accordingly, for each interferogram we first apply the ESD procedure to the range-overlapped zones of each burst and the misregistration error Δt_j^{res} for the jth interferograms is estimated as follows:

$$\Delta t_j^{\text{res}} = \frac{1}{2\pi\kappa} \sum_{(x,r)\in\Gamma} \frac{\Delta\phi_j^{\text{res}}(x, r)}{\Delta f(x, r)} \tag{7}$$

where Γ represents the set of pixels showing a spatial coherence value greater than a fixed threshold γ (typically 0.5) and κ is the number of elements of this set.

Following the estimation of the vector $\mathbf{\Delta t^{res}} = [\Delta t_0^{\text{res}}, \ldots, \Delta t_j^{\text{res}}, \ldots, \Delta t_{M-1}^{\text{res}}]$, the shifts of each SAR acquisition with respect to the master image, say $\mathbf{t^{res}} = [t_0^{\text{res}}, \ldots, t_i^{\text{res}}, \ldots, t_{N-1}^{\text{res}}]$, are easily retrieved by following the same procedure applied for the rigid offset estimation [see (2)–(4)].

The same estimation procedure (Fig. 5) is then applied to the azimuth overlapping regions between adjacent bursts (purple area in Fig. 6). Accordingly, we may finally compute the azimuth residual misregistration errors, with respect to the master image geometry, by jointly exploiting the results obtained through the ESD method applied to both range and azimuth overlapping regions between the adjacent bursts (light blue and purple areas in Fig. 6, respectively).

The estimated misregistration values, say $\overline{\mathbf{\Delta t}}^{\boldsymbol{res}} = [\overline{\Delta t}_0^{\text{res}}, \ldots, \overline{\Delta t}_j^{\text{res}}, \ldots, \overline{\Delta t}_{M-1}^{\text{res}}]$, are finally retrieved as follows:

$$\overline{\mathbf{\Delta t}}^{\boldsymbol{res}} = \mathbf{A} \times \mathbf{t^{res}} \tag{8}$$

and are exploited to filter out the residual phase ramps directly from the burst interferograms, following (5). Indeed, it is worth noting that the result of the twofold (range and azimuth) ESD procedure is not used to coregister again the bursts of the multitemporal images sequence deriving from the burst images coregistration step (Fig. 5), in order to account for the residual azimuth mis-registration errors. Indeed, such errors are of a few hundredths of sample and, therefore, they do not have a significant impact on the spatial coherence of the interferograms. Accordingly, there is no need for a second coregistration step and the estimated residual azimuthal misregistration shifts are exploited to estimate the phase ramps that are directly removed from the already available burst interferograms.

IV. S-1 IW P-SBAS Processing Chain

This section concerns the overall description of the P-SBAS interferometric chain developed to efficiently process the S-1 IW multitemporal SAR data sets.

It is worth noting that the workflow, the general algorithmic structure, and the parallelization rationale of the presented S-1 interferometric processing chain follow those implemented within the original P-SBAS approach [42]. Note also that although it was not conceived for a specific SAR system, the original P-SBAS processing chain was at first designed to handle multitemporal stripmap SAR data sets by effectively exploiting distributed computing infrastructures (i.e., grid and CC platforms); over time, this solution has been thoroughly tested in different hazard contexts by processing both ENVISAT and COSMO-SkyMed SAR data [44], [64], [73]. Here, we mainly focus on the innovative steps that have been introduced within the P-SBAS processing chain to proficiently handle the S-1 IW SAR data which, as extensively discussed before, require specific solutions to be implemented for efficiently tackling the peculiarities that characterize the TOPS acquisition mode.

The main modifications of the developed S-1 P-SBAS processing chain, for what concerns the parallelization strategy, regard the achievement of a deeper granularity level with respect to the stripmap mode one [42], which derives from the burst partitioning characterizing the S-1 IW data structure. Indeed, for each SAR scene it is possible to collect a set of independent bursts that can be handled and processed as separate images, from the input data ingestion up to the DInSAR interferograms generation, thus fostering the intrinsic parallelization of the S-1 IW interferometric processing on a burst basis. This can be automatically carried out through the exploitation of efficient algorithms and high-performance distributed computing infrastructures for tackling the arising huge data flow. It is worth noting that similar to the original stripmap case, the developed S-1 IW P-SBAS processing chain exploits different granularity parallelization strategies, which require the use of both multinode and multicore programming techniques to deal with the hardest computationally steps. In addition, we further remark that the processing chain does not encompass the starting raw data-focusing step included in the original stripmap one; indeed, the presented S-1 P-SBAS implementation accounts for the exploitation of SLC products, only; however, the integration of a TOPS raw data focusing block could be easily accomplished within the developed solution, with no significant impact on the overall processing scheme.

The block diagram in Fig. 7 schematizes the overall workflow of the implemented S-1 IW P-SBAS processing chain. As mentioned before, the original P-SBAS implementation is here mostly preserved; nevertheless, an algorithmic improvement, already discussed in Section III and relevant to the accurate burst interferograms generation procedure, is carried out. Moreover, following the burst interferograms mosaicking operation, two additional processing steps are included. The first one implements an interferograms noise filtering procedure [74] which permits, by properly exploiting the temporal relationships among the generated redundant set of SB interferograms [see (1)], to significantly mitigate their noise effects; more specifically, this is based on the pixel-by-pixel solution of a nonlinear minimization problem involving the phase information of the exploited multilook

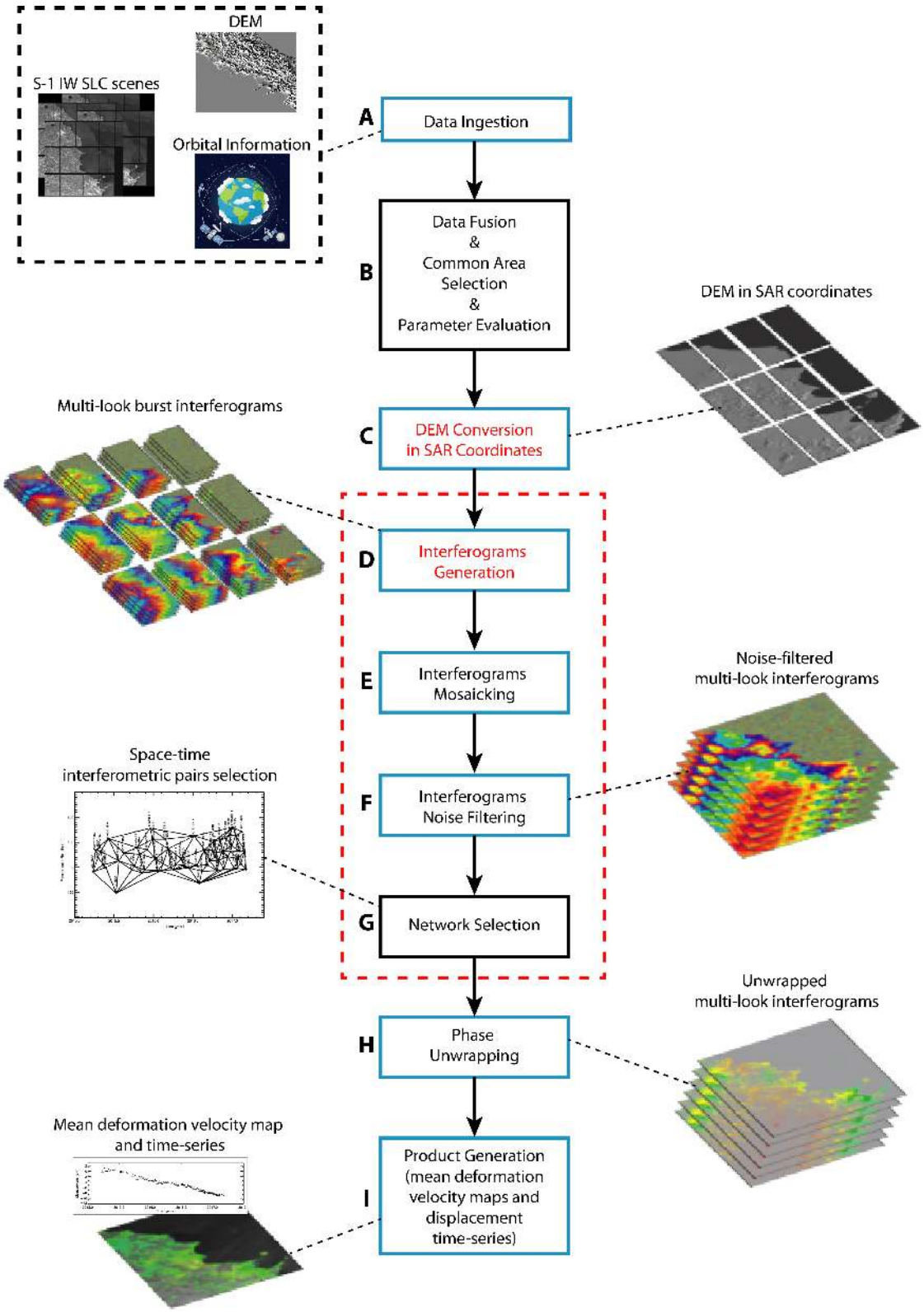

Fig. 7. S-1 IW P-SBAS processing chain workflow. The black blocks represent the sequentially executed steps, whereas the blue ones indicate the parallel computed operations; the procedures that benefit from a burst granularity parallelization level are highlighted in red. Moreover, the dashed red line groups the new steps or those that underwent the main modifications with respect to the original (strimap) P-SBAS implementation.

DInSAR interferograms. The second step implements a selection, among all the generated SB interferometric pairs, of an optimized triangular network within the perpendicular-baseline/time plane [75], to be used for the phase unwrapping (PhU) operations and the subsequent LS solution retrieval that characterizes the SBAS approach [8]. Note that new steps or those that underwent the main modifications of the developed S-1 IW P-SBAS processing chain

are schematically grouped with the dashed red box depicted in Fig. 7.

It is also worth noting that the black and blue colors used to highlight different blocks shown in Fig. 7 allow us to easily discriminate the processing steps that are intrinsically sequential from those where the concurrent jobs are executed in parallel (by exploiting both multiple nodes/CPUs and multithreading programming techniques, depending on the input data and on the computational load for each specific step). Among the latter, the steps that benefit from the burst partitioning granularity, which represent the key enhancement of the parallelization strategy of the implemented S-1 processing chain, are marked by red color texts.

We now address a concise description of the blocks reported in Fig. 7, without deepening the algorithmic solutions and the parallelization strategies adopted for each step. Indeed, a detailed analysis on the computational load and different parallelization solutions exploited for each processing block of the P-SBAS approach can be found in [76].

The first block represented in the processing chain workflow (Step A in Fig. 7) concerns the ingestion and unpacking operations performed on the input SAR data, which consist in a sequence of temporally separated S-1 IW SLC images over the area of interest, the corresponding orbital information, as well as the precise digital elevation model (DEM) of the overall investigated area. Among the implemented operations, this step accounts for suitable corrections of possible artifacts present in the amplitude and/or phase signals of the SLC images and introduced by different Instrument Processing Facilities (IPFs) released during the Sentinel-1 system lifetime. This block is carried out in parallel with a granularity level based on the single SLC.

Once the input data are correctly ingested, Step B performs a series of sequentially executed operations, consisting in the selection of the master image to take as a reference geometry for the registration of the entire SAR data set, the area of interest common to the whole SLCs, as well as the actual bursts to be processed. Moreover, if more than one S-1 slice per SAR acquisition fall within the area of interest, Step B carries out the operations to fuse azimuthal-adjacent S-1 SLC slices together. Finally, to be in line with the subsequent burst coregistration step of the workflow, Step B implements a first selection of the possible interferometric data pairs involving the available SAR acquisitions. In particular, each SAR image is initially paired with the following (in time) six acquisitions (whenever available) to produce the list of the interferometric SAR data pairs to be exploited within the subsequent interferograms generation (Step D in Fig. 7) and interferograms noise filtering (Step F) operations. Note that, since we fully benefit from the intrinsic SB characteristics of the S-1 constellation, no perpendicular baseline constraint is applied within the interferometric pair selection.

The conversion of the available DEM into the radar (azimuth and range) coordinates through the so-called range-Doppler equations [77] is performed in Step C, followed by the estimation, for each pixel of the exploited SAR images, of both range and azimuth target-to-sensor distances with respect to the master orbital position, referred to as range and azimuth matrices [70]. This step is parallelized on a burst level, but it also supports a further partitioning of the initial DEM matrix into patches smaller than the bursts [42].

As previously anticipated, Step D is relevant to the most innovative block of the developed S-1 P-SBAS processing chain, which is parallel executed at burst level. In particular, Step D concerns the coregistration of each burst of the SLC images with respect to the master acquisition geometry, the burst interferogram generation and subsequent correction, extensively discussed in Section III. Note that a spatial complex average (multilook) operation [5] is carried out to mitigate the decorrelation noise effects [23] within the generated interferograms and to reduce the amount of data to process.

In the following block, the corrected multilook interferograms and corresponding spatial coherence maps of adjacent bursts are accurately put together through an interferogram mosaicking operation (Step E), in order to generate the differential interferograms of the whole investigated area.

Once these interferograms are generated, the workflow addresses the previously mentioned interferogram noise filtering [74] and network selection [75] operations in Steps F and G, respectively. In particular, the interferogram noise filtering procedure is executed according to a pixel granularity parallelization level, by exploiting multinode programming techniques, to efficiently manage its large computing load, whereas the selection of an optimized reduced network of time-redundant interferograms forming a triangulation in the temporal/perpendicular baseline domain is sequentially carried out.

Step H performs the temporal and spatial PhU operations by applying the EMCF algorithm [78] on the sequence of SB interferograms belonging to the previously selected optimized network. In particular, the EMCF algorithm is applied to a subset of pixels identified by selecting those characterized by a triangular coherence value (see Appendix) greater than a fixed threshold (in this paper, we assume that is equal to 0.85). This step allows retrieving the final sequence of unwrapped multilook interferograms by making use of both multinode and multithreading parallelization strategies [79].

The generation of the displacement time series and the corresponding mean deformation velocity maps is accomplished in the last block of the S-1 IW processing chain workflow. In particular, Step I performs the inversion of the retrieved sequence of unwrapped interferograms by searching for an LS solution. In addition, this step computes the temporal coherence factor [78] to provide a measurement of the reliability of the achieved results and filters out possible undesired atmospheric artifacts from the displacement time series [8]. Step I operations are executed according to a parallelization strategy with a pixel granularity.

The workflow shown in Fig. 7 and described in this Section is suitable for the implementation within CC environments. In particular, it is worth noting that to migrate the developed processing chain into CC infrastructures, we leverage the advancements and the innovative strategies discussed in [42]–[45], which focused on the analysis of the P-SBAS parallel performances and scalability within CC environments. The achieved performance, obtained by migrating the

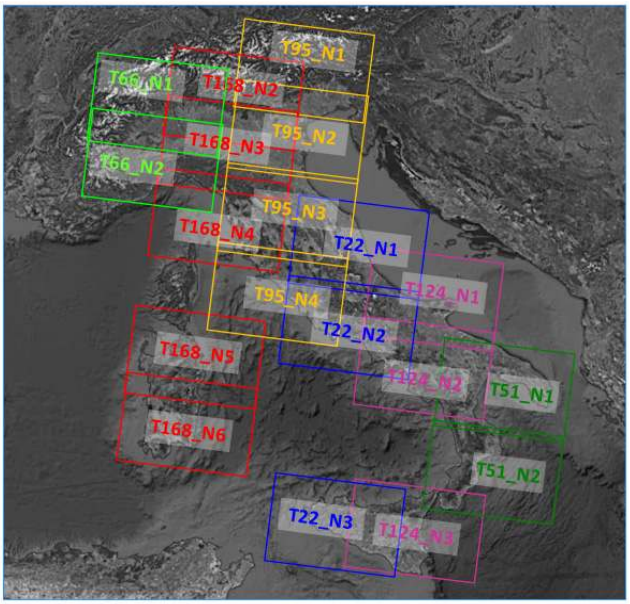

Fig. 8. Optical image of the Italian territory with superimposed the representation of the 19 S-1 frames, acquired from descending orbits and processed through the implemented S-1 IW P-SBAS processing chain. Note that each color identifies a different track.

implemented S-1 IW processing chain within the AWS CC environment, is discussed in Section V.

V. Experimental Result Analysis

In order to assess the quality of the interferometric products generated through the implemented P-SBAS processing chain and to investigate its performance within a CC environment, we exploited the whole archive of S-1 SLC images acquired from descending orbits over Italy between March 2015 and April 2017. In particular, the considered data set includes six different descending tracks (66, 168, 95, 22, 124, 51) divided into 19 frames (see Fig. 8); the total number of processed S-1 slices is 2740 corresponding to a total number of 1281 S-1 acquisitions (see Table I).

In the following, we present the results of our analysis carried out on such a large data set.

A. Interferograms Quality Assessment

The S-1 IW interferograms are obtained by applying the approach presented in Section III to the selected interferometric data pairs; this led to process 7287 interferometric data pairs and to generate the corresponding differential interferograms. Note also that in the interferogram generation operation, we exploited the 1-arcsec Shuttle Radar Topography Mission (SRTM) DEM to remove the topography-related phase components and then we performed a complex multilook operation with 20 looks in the range direction and five looks in the azimuth one, thus obtaining a pixel dimension of about 70 m $\times$ 70 m. Moreover, no spatial baseline constrain was imposed thanks to the narrow orbital tube characterizing the S-1 constellation (see Fig. 4).

TABLE I
Characteristics of the Exploited S-1 Data Sets Over the Italian Territory

Frame	Number of S-1 slices	Number of S-1 acquisitions
T66_N1	128	71
T66_N2	186	71
T168_N2	128	72
T168_N3	119	68
T168_N4	135	67
T168_N5	154	67
T168_N6	116	66
T95_N1	128	64
T95_N2	144	64
T95_N3	130	65
T95_N4	130	65
T22_N1	155	66
T22_N2	160	67
T22_N3	120	66
T124_N1	134	67
T124_N2	177	67
T124_N3	184	72
T51_N1	138	68
T51_N2	174	68
Total	**2740**	**1281**

In order to assess the accuracy of the implemented interferograms generation procedure, we considered the final (phase-compensated) differential interferograms and investigated the standard deviation values of the residual phase variations (jumps) following the burst interferograms compensation step (Fig. 5). In particular, for each interferogram, we retrieved the standard deviation value of the phase difference [expressed in samples by considering (5)] computed in the overlapping regions between azimuth-adjacent bursts (purple area in Fig. 6).

As a first result, we present in Fig. 9 the histogram of the retrieved standard deviation values associated with the overall interferograms. We highlight that only seven interferograms out of the generated 7287 (less than 0.1%) show a standard deviation value greater than 5×10^{-3} samples, being the maximum computed value equal to 5.4×10^{-3} samples; moreover, 96% of the interferograms (6989) have a standard deviation value smaller than 3×10^{-3} samples (87% smaller than 2×10^{-3} samples).

These results show that the very high accuracy achieved thanks to the implemented interferograms generation procedure.

Moreover, we remark that most of the interferograms (200 out of 298) showing standard deviation values greater than 3×10^{-3} samples are generated from interferometric pairs where only one of the two SAR acquisitions was produced with the IPF version labeled as 2.6.X, while the same effect is largely less important when master and slave images of the interferometric pairs are both produced with this or any other IPF release/version.

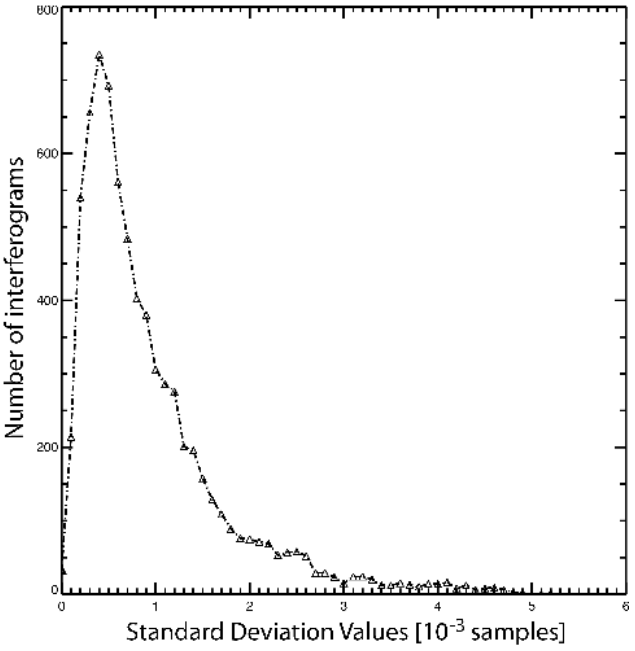

Fig. 9. Histogram of the standard deviation values of the residual phase differences (expressed in samples), following the burst interferograms correction step of Fig. 5, estimated for each interferogram in the overlapping regions between azimuth-adjacent bursts.

To better clarify this issue, we investigate in Fig. 10 the standard deviation values of the interferograms relevant to different processed frames. In particular, each diagram in Fig. 10 shows the standard deviation values computed for all the interferograms of a considered frame; note that the X- and Y-axes represent the acquisition dates of the master and slave images of the interferometric pairs, respectively, while the diamonds indicate the computed interferograms. The color associated with each diamond represents the standard deviation value of the residual phase jumps (expressed in samples) between azimuth adjacent bursts of the interferogram, whereas the continuous black lines indicate the starting (end of November 2015) and ending (mid-April 2016) dates relevant to the use of the IPF version 2.6.X. The impact of this IPF version is evident because it clearly introduces an artifact within the corresponding interferograms. This effect is very likely due to the incompatibility of this IPF release with respect to other previous or subsequent versions [80].

B. Processing Chain Result Quality Assessment

An extensive analysis on the quality assessment of the deformation time series obtained by applying the developed S-1 IW P-SBAS processing chain is here carried out. Also in this case, equivalently to the performance analysis carried out on the interferograms generation procedure, we exploited the whole archive of S-1 SAR data collected over Italy between March 2015 and April 2017, already detailed in Fig. 8 and Table I. This large data set was processed with the implemented P-SBAS processing chain presented in Section IV and the achieved deformation time series were validated by exploiting independent *in situ* measurements.

To provide an overall view of the obtained results, we first present in Fig. 11 the geocoded mean deformation velocity map of the 19 processed frames, superimposed on an optical image of Italy, computed with a ground spacing of about 70 m both in the azimuth and range direction.

The displayed velocity map covers an area of about 300 000 km^2 and provides information on the temporal evolution of about 23 millions of coherent pixels. These were identified by benefiting from the temporal coherence factor [78] that provides an estimate of the quality of the obtained results on the pixels where the deformation time series are properly retrieved. In particular, we assume as coherent pixels those characterized by a temporal coherence value greater than a selected threshold equal to 0.9; clearly, the zones exhibiting lower values of the temporal coherence threshold were masked out in Fig. 11.

The velocity map of Fig. 11 shows a large variety of deformation phenomena with the most evident one represented by the well-known displacement pattern associated with the seismic crisis that stroke Central Italy between August 2016 and January 2017, and which was already extensively investigated [68], [69]. Accordingly, to investigate the surface displacement retrieval capability of the implemented P-SBAS chain, we consider four selected zones affected by significant deformation patterns, highlighted in Fig. 11 by the red squares labeled as (a), (b), (c) and (d), and zoomed in Fig. 12. In particular, in Fig. 12(a), we report a sketch of the mean deformation velocity map relevant to the Pistoia-Prato Plain (Northern Italy) where a subsidence phenomenon, mainly related to the large amount of ground-water pumped for the industrial activities carried out in this area [81], is evident. Furthermore, we report the LOS-projected displacement time series relevant to a selected pixel (labeled as P1 in Fig. 12(a) and marked by a black star), located in the maximum deforming zone; it shows a clear subsidence signal on which a seasonal oscillation is superimposed.

Fig. 12(b) depicts a zoomed-in view of the mean deformation velocity map of Fig. 11 relevant to the Fiumicino Airport and surroundings (Southwest of the urban area of Rome, in central Italy). In this case, the map reveals a spatially extended subsidence pattern related to the interaction between natural and man-induced causes, i.e., compaction of unconsolidated sediments and progressive urbanization [82]. The observed deformation pattern is characterized by a deformation rate up to 2 cm/year, clearly shown by the temporal evolution of the displacement reported for the pixel labeled as P2 and identified with a black star in Fig. 12(b).

Fig. 12(c) highlights a sketch of the mean deformation velocity map relevant to the area surrounding the little town of Maratea (Southern Italy), which is interested by extended landslide phenomena [83]. The corresponding plot ([Fig. 12(c)] shows the temporal evolution of the retrieved LOS-projected deformation, characterized by a cumulative displacement value of about 4 cm measured in the overall observation period for the pixel labeled as P3 and identified with a black star in [Fig. 12(c)].

Finally, Fig. 12(d) reports a zoomed-in view of the mean deformation velocity map of Fig. 12 relevant to the

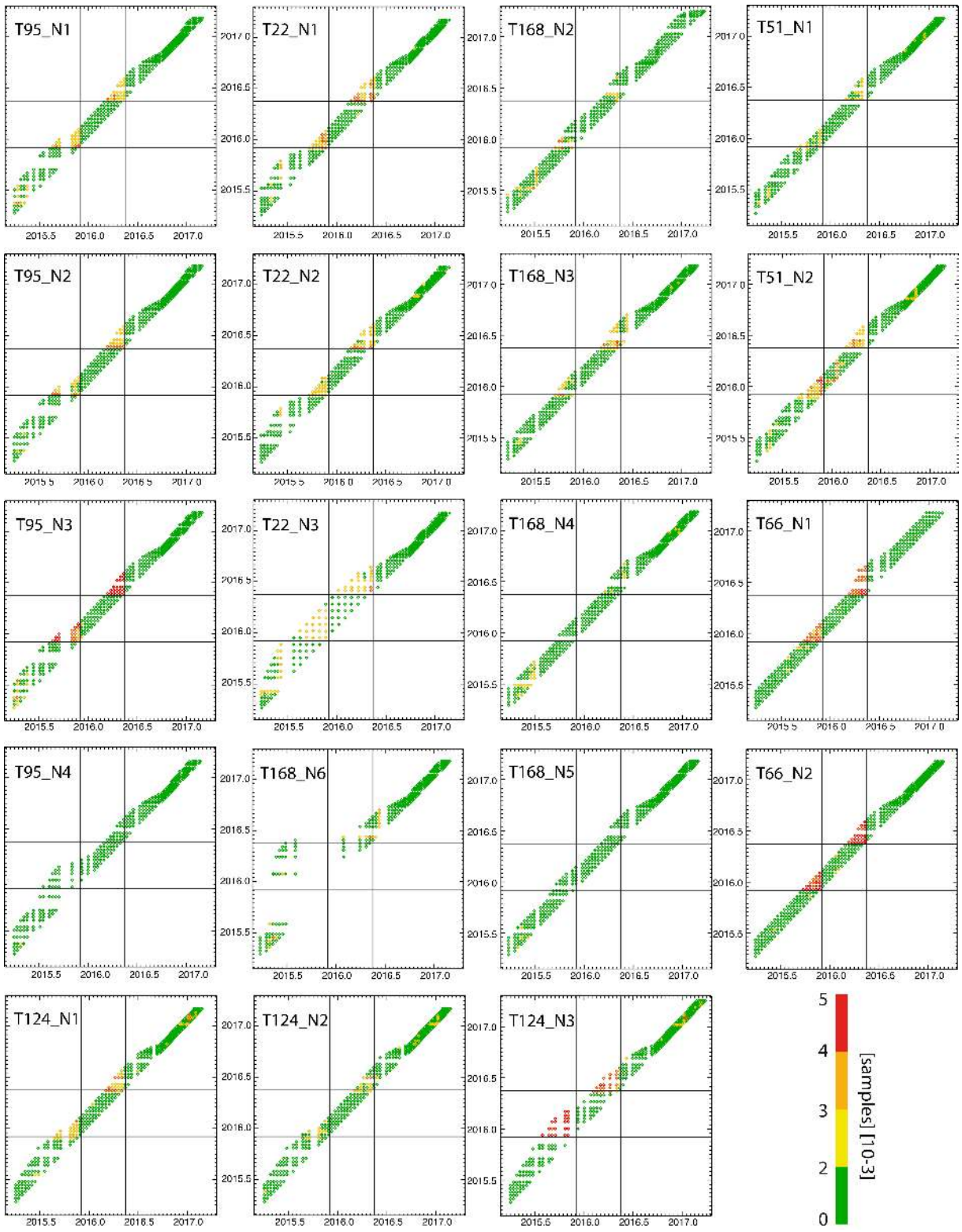

Fig. 10. Standard deviation values computed for all the interferograms of the processed frames; the X- and Y-axes represent the acquisition dates of the master and slave images of the interferometric pairs, respectively, whereas the diamonds indicate the computed interferograms. The color associated with each diamond represents the standard deviation value of the residual phase jumps (expressed in samples) between azimuth-adjacent bursts of the interferogram, whereas the continuous black lines indicate the starting and ending dates relevant to the use of the IPF version 2.6.X.

Campi Flegrei caldera (Southern Italy), a well-known active volcanic zone close to the Naples city (Southern Italy), which has been experiencing an almost continuous uplift of the ground surface since late 2005 [84]–[89]. Moreover, we present the plot of the displacement time series of a pixel located in the area of maximum deformation of the caldera,

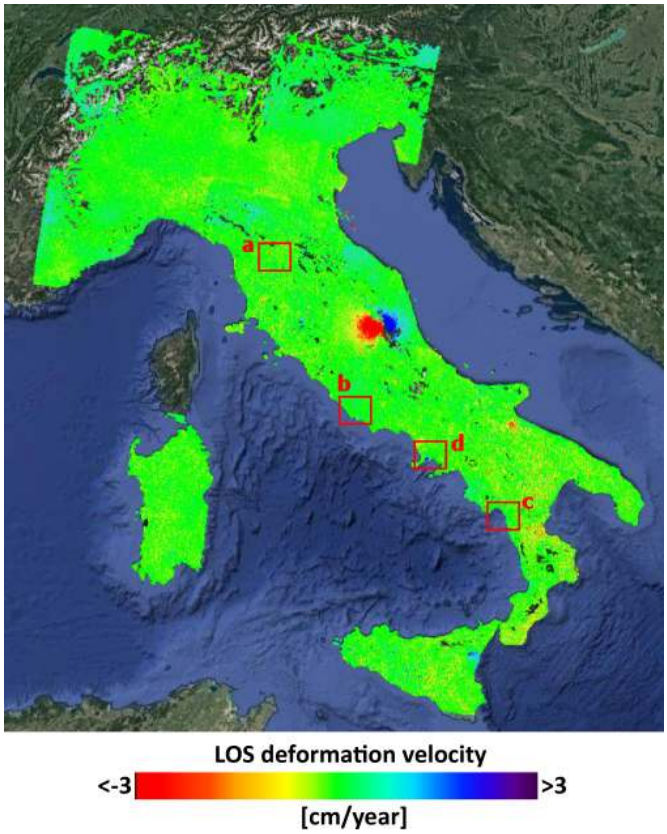

Fig. 11. LOS mean deformation velocity map (cm/year), geocoded and superimposed on an optical image of Italy. The four red squares identify four selected zones characterized by significant deformation phenomena: (a) Prato-Pistoia Plain, (b) Fiumicino Airport, (c) Maratea landslide, and (d) Campi Flegrei Caldera, respectively. The deformation phenomena relevant to these areas are deeply investigated in Fig. 12.

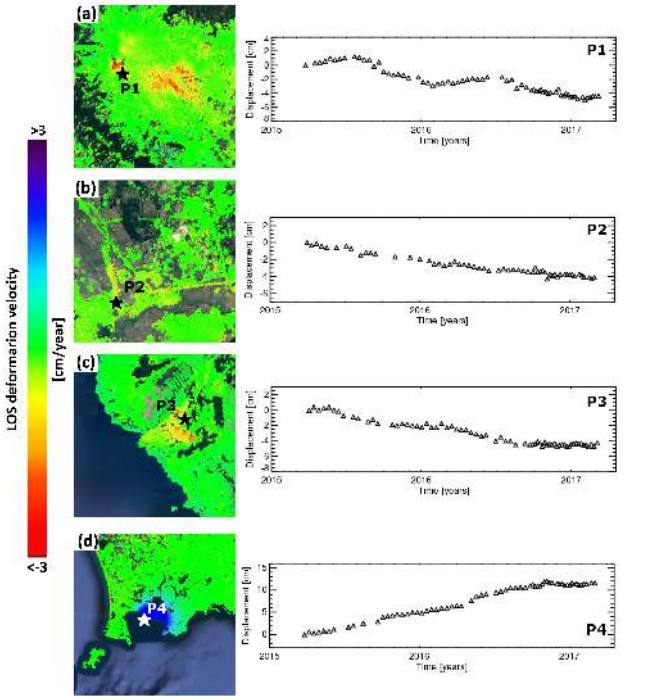

Fig. 12. (Left) Zoomed-in views of the four areas identified in Fig. 11 by the red squares labeled as (a)–(d). (Right) LOS-projected displacement time series relevant to pixels, marked by the stars in the maps, located in the maximum deforming areas. (a) Mean deformation velocity maps related to (a) Prato-Pistoia Plain, (b) Fiumicino Airport zone, (c) Maratea town, and (d) Campi Flegrei caldera and associated deformation time series of the pixel labeled as P1, P2, P3, and P4.

highlighted with a white star and labeled as P4 in Fig. 12(d). The temporal evolution of the displacement for the selected pixel shows the nonlinear deformation behavior characterizing the caldera; indeed, we first observe an LOS-projected displacement evolution exceeding 10 cm; subsequently, starting from August 2016, a significant decrease of the deformation rate is retrieved.

Let us now investigate the performance of the implemented P-SBAS processing chain for what concerns the accuracy of the generated deformation time series. To this aim, we compared the achieved P-SBAS results with the available geodetic measurements that are assumed as reference. The analysis is first focused on the above-mentioned Campi Flegrei Caldera (Southern Italy) and, subsequently, on the whole Italy, by benefiting from the availability of the GPS time series provided by the INGV-OV and UNR-NGL. In the first case, we exploited the weekly position time series of the Neapolitan Volcanoes Continuous GPS (NeVoCGPS) network, managed by the INGV-OV since the beginning of 2000s [90], [91]. Presently, it consists of about 50 permanent stations (25 within the Campi Flegrei area) distributed in the Neapolitan volcanic district and surrounding area. Moreover, we further extended the P-SBAS quantitative assessment analysis by also exploiting the GPS measurements provided by the UNR-NGL in the framework of the "Plug and Play GPS" Project [92] which processes all the openly available GPS data, currently from over 14 000 continuously operating stations from around the globe; in particular, for the Italian territory, we have selected the GPS daily time series of about 700 stations.

For what concerns the Campi Flegrei Caldera, in Fig. 13(a), we show a sketch of the mean deformation velocity map of Fig. 11 [same zoomed-in view of Fig. 12(d)] and in Fig. 13(b), the Google base map of the area with highlighted the locations of the OV-INGV GPS stations (blue and red dots) installed in the area. Moreover, in Fig. 13(c)–(h), we present some plots showing the comparisons between the displacement time series retrieved through the developed S-1 IW P-SBAS processing chain (black triangles) and the corresponding LOS-projected GPS ones (red stars), for the stations labeled in Fig. 13(b) as ARFE, STRZ, RITE, ACAE, IPPO and NISI, respectively. Consistently with previous results [18], [50], there is a very good agreement between the P-SBAS and LOS-projected GPS measurements. For each station of the NeVoCGPS network located in correspondence to a DInSAR coherent pixel, we computed the standard deviation value of the difference between the two time series in the temporal window common to both measurements; the obtained results, relevant to 42 stations located in correspondence of coherent pixels within the S-1 IW interferograms, are reported in Table II. Based on these measurements, we also calculated the average standard deviation of the difference between the DInSAR and the GPS time series, obtaining a value of 0.35 cm.

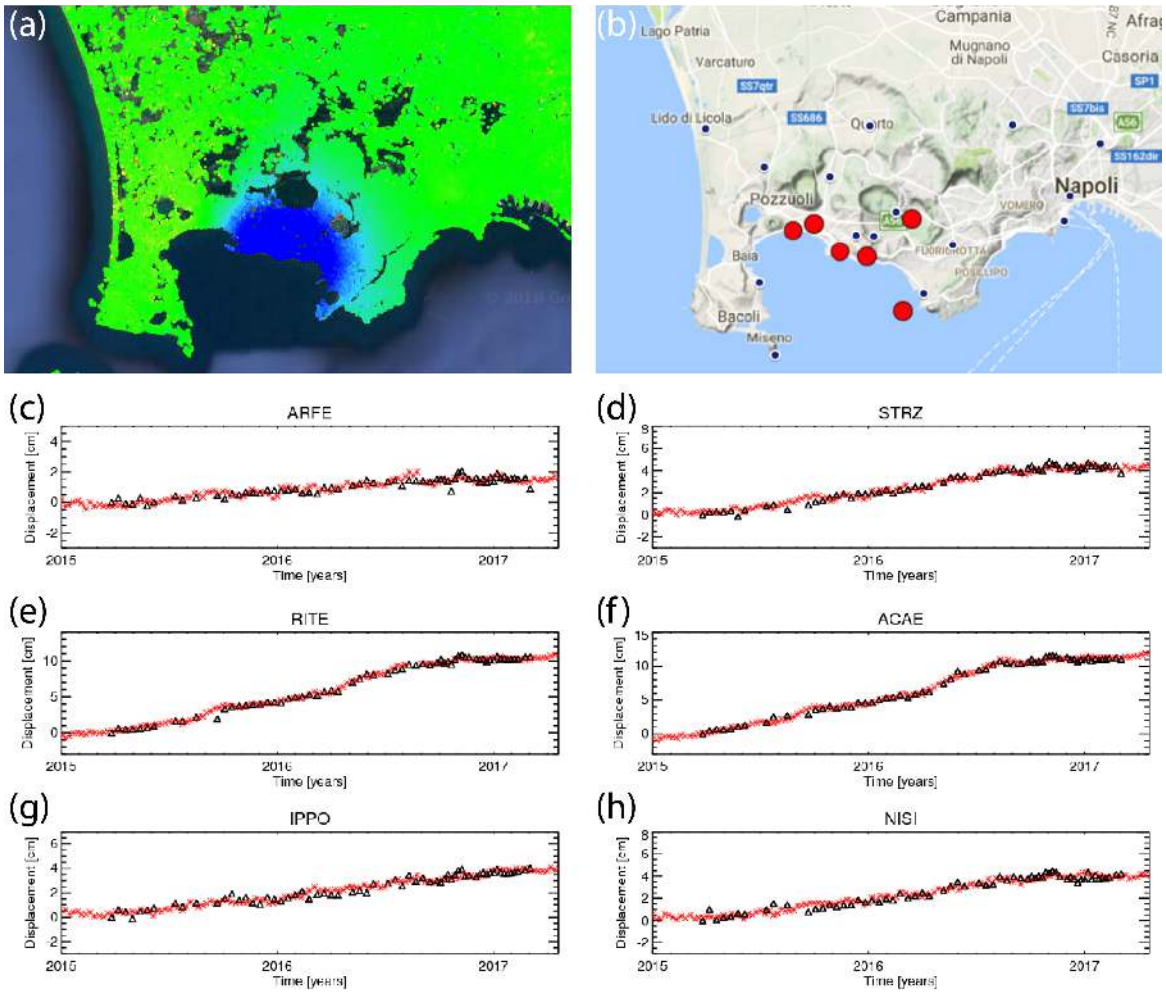

Fig. 13. (a) Zoomed-in view of the mean deformation velocity map of the Campi Flegrei Caldera [same as Fig. 12(d)]. (b) Google base map of the Campi Flegrei Caldera with highlighted the locations of the GPS stations (blue and red dots) belonging to the OV-INGV GPS network. (c)–(h) Comparison between the P-SBAS (black triangles) and the LOS-projected GPS (red stars) surface deformation time series relevant to the stations identified in panel (b) through the red dots and labeled as ARFE, STRZ, RITE, ACAE, IPPO, and NISI, respectively.

For what concerns the analysis relevant to the overall Italian country, we show in Fig. 14 a Google base map with highlighted the positions of the selected GPS stations (blue and red dots) for which we exploited the measurements available through the UNR-NGL data processing. These GPS stations are those located in coherent areas of the DInSAR velocity map of Fig. 11, and for which the GPS measurements are available for at least 1.5 years, thus ensuring a good overlap with the available S-1 data. Following the GPS selection, which leads to analyze a total number of GPS stations equal to 434, we carried out an extensive comparison between the homologous P-SBAS and LOS-projected GPS time series. To this aim, all the measurements (SAR and GPS) were computed with respect to a GPS reference station chosen for each S-1 SAR frame among those located in correspondence to coherent pixels.

We started this analysis by first carrying out a comparison between the P-SBAS and LOS-projected GPS displacements on a selection of 12 GPS sites with a rather uniform distribution on the whole Italian territory and characterized by different features in their deformation time series. These stations are those identified by the red dots of Fig. 14 and are labeled as PIAC, PARM, SERM, CECI, ANC3, AQUI, MOSE, PTRJ, ALB5, UGEN, CROT, and TAOR, respectively. For each of these stations, we compared the P-SBAS results (black triangles) with the corresponding LOS-projected GPS measurements (red stars) available within the SAR acquisition window. The results of these comparisons are depicted in the plots of Fig. 15, clearly showing the good agreement between these two sets of measurements.

Following these results, we focused on an extended quantitative assessment of the P-SBAS measurements quality. Accordingly, for all the 434 selected GPS stations, we computed the standard deviation values of the difference between the P-SBAS and LOS-projected GPS time series. To this aim, being the UNR-NGL time series themselves affected by noise (although they are assumed as reference), we considered a smoothed version of the GPS time series in the period common to the SAR acquisitions. The achieved results are summarized in the Fig. 16; note that about 70% of the standard deviation

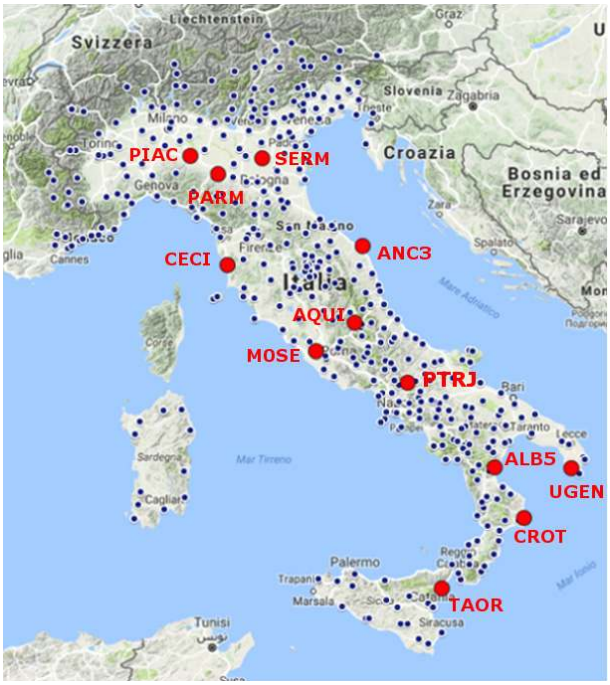

Fig. 14. Google base map of Italian territory with highlighted the locations of the GPS stations (blue and red dots) exploited through the UNR-NGL "Plug and Play GPS" Portal.

TABLE II

RESULTS OF THE COMPARISON BETWEEN THE P-SBAS AND THE LOS-PROJECTED GPS DEFORMATION TIME SERIES RELEVANT TO THE NEAPOLITAN VOLCANIC AREA (CAMPI FLEGREI CALDERA, VESUVIUS AND ISCHIA ISLAND)

GPS Station	Standard deviation		**GPS Station**	Standard deviation
ACAE	0.30		MORU	0.30
AGR1	0.23		NAMM	0.18
AQMO	0.34		NAPO	0.21
ARFE	0.24		NISI	0.32
ASTR	0.21		ONPI	0.29
BAGN	0.26		OSCM	0.34
BAIA	0.34		OSVE	0.55
BKE1	1.10		PACA	0.26
BKNO	0.70		PAOL	0.40
CMIS	0.22		PIGN	0.31
ENAV	0.62		PIS1	0.31
FISC	0.23		PRET	0.31
FORI	0.40		QUAR	0.22
FRUL	0.27		RITE	0.29
IPPO	0.27		SANA	0.32
IPRO	0.29		SANT	0.49
ISCH	0.69		SERR	0.50
ISMO	0.21		SOLO	0.29
LICO	0.29		STRZ	0.27
MAFE	0.19		TERZ	0.48
MODR	0.41		VICA	0.28
Average standard deviation value: 0.35 cm				

values relevant to the differences between the DInSAR and the LOS-projected GPS measurements is smaller than 0.5 cm, while less than 1% is greater than 1 cm. Moreover, we also computed the average standard deviation value relevant to the differences between the two data sets, which corresponds to about 0.44 cm (see red dotted horizontal line in Fig. 16); note that this value is consistent with what previously found through the analysis of the SBAS products obtained thanks to the first generation SAR sensors [18], [19].

Summing up, the presented analysis clearly demonstrates the capability of the implemented P-SBAS processing chain to retrieve, from S-1 IW SAR data sets, displacement time series with sub-centimetric accuracy. In particular, the mean standard deviation value of the differences between the DInSAR and the GPS measurements can be reliably assumed to be less than 0.5 cm.

C. Processing Chain Performance Assessment Within a CC Environment

This paragraph is aimed at concisely describing the performance, in terms of elapsed computing times, of the CC implementation within the AWS environment of the S-1 IW P-SBAS processing chain presented in this paper.

It is worth noting that the potentialities of the exploitation of CC environments for the massive processing of S-1 IW data, through the P-SBAS approach, were already thoroughly discussed in [76], where we focused on the capability to perform large scale (continental) interferometric analyses exploiting in parallel the AWS resources.[3] However, in [76], a simplified version of the S-1 IW P-SBAS processing chain was exploited.

Accordingly, in the following analysis, we first briefly recall the main information on the implementation of the S-1 IW P-SBAS processing chain within the AWS Elastic Cloud Compute (EC2) platform [94] and, subsequently, we focus on the achieved performances, i.e., the elapsed times relevant to the complete P-SBAS processing, referring to the overall workflow shown in Fig. 7. To this aim, we selected an S-1 IW frame that can be considered as a reference one.

In order to efficiently exploit the AWS resources for the S-1 IW P-SBAS processing, we implemented.

1) An S-1 IW data archive located on the Simple Storage Service (S3) of AWS [95], which is a long-term storage having a theoretically infinite network bandwidth in connection to the computing nodes of the AWS EC2. The created archive currently contains all the S1 IW SLC images acquired over Italy and is updated with new acquisitions every time new data on the S-1 catalog [96] are available;
2) An automatic pipeline able to exploit in parallel the AWS EC2 resources for processing S-1 IW data through the P-SBAS processing chain described in Section IV, which starts with the transfer of the data from the above-mentioned archive on S3 storage to the EC2 computing nodes exploited for the computation, then launches the data processing in parallel on these computing nodes and finally performs the upload of the generated interferometric results on a dedicated space of the S3 AWS storage for their long-term preservation.

[3]Note that other publicly available AWS tools for S-1 interferometric processing can be found in [93]

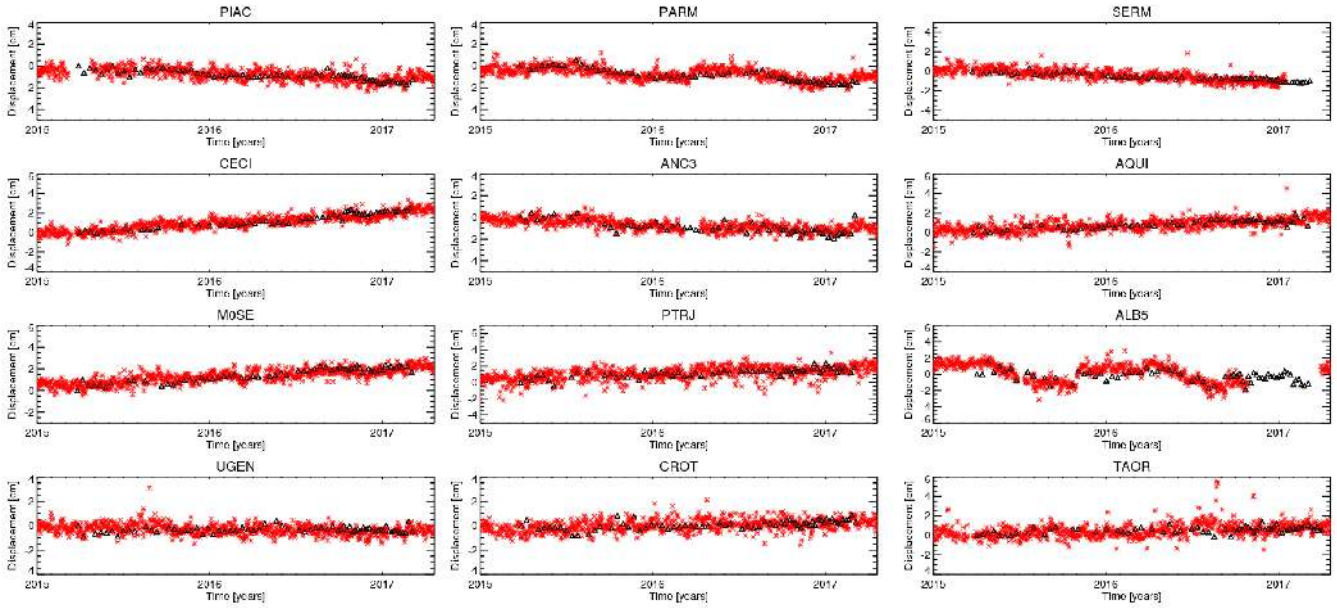

Fig. 15. Comparison between the P-SBAS (black triangles) and the LOS-projected GPS (red stars) surface deformation time series relevant to the stations of the GPS stations identified in Fig. 14 by the red dots and labeled as PIAC, PARM, SERM, CECI, ANC3, AQUI, M0SE, PTRJ, ALB5, UGEN, CROT, and TAOR, respectively.

The overall pipeline is written in bash scripts, also exploiting the AWS Command Line Interface (CLI) for the operations that involve the management of the AWS CC resources, such as the data download/upload from/to S3 and the launch/stop of the AWS instances (i.e., the computing nodes) [45], [64], [76]. It ingests as input the list of S-1 IW SLC images to be processed and, if requested, the vertexes of the area of interest to be analyzed; the pipeline performs, in a fully automatic way, all the actions relevant to the data download from the S3 AWS archive, the launch of the P-SBAS processing and the storage of the results. Note that the developed pipeline is also able to automatically handle the processing of several independent S-1 IW frames in parallel, through different AWS instances [45], [76]. We further remark that the majority of the P-SBAS processing chain algorithms are developed in the Exelis Interactive Data Language (IDL); moreover, there are also parts of the code written in Fortran and C programing languages.

Concerning the management of the parallel processing on the AWS CC resources, i.e., the scheduling of the P-SBAS parallel tasks among different computing nodes and/or cores, it is worth noting that, as explained in Section IV, different parallelization strategies are adopted throughout the several steps of the processing chain depending on both the implemented algorithms and the input data, including multinode and multithreading programing techniques. This information is thoroughly detailed and discussed in [76]; we here recall that the overall parallel jobs scheduling is handled by means of a package of bash scripts able to distribute the concurrent jobs both among multiple computing nodes and multiple cores within each computing node.

As a reference for the evaluation of the elapsed processing times we selected the S-1 IW frame labeled as T22_N2 in Fig. 8 and Table I, covering an area that includes the Naples Bay and extends up to the city of Rome. The selected frame

TABLE III
i3.16XLARGE INSTANCE CHARACTERISTICS

i3.16xlarge instance characteristics	
vCPU	64
RAM	488GB
Internal Storage	15.2 TB (8xNVMe SSD)
Network Bandwidth	25 Gbps

can be considered as a reference one, because the mapped area extends for approximately 250×250 km^2 and the overall SAR data set consists of 160 S-1 IW SLCs, i.e., it includes all the available acquisitions between March 2015 and April 2017. Note that after the fusion of the SLCs acquired in the same dates we finally obtain 67 scenes. The total number of bursts to be processed, according to the crop performed on the area of interest, is 2624 and the number of generated interferograms is 381. As a consequence, the size of the input data set is of about 1.2 TB, whereas the storage required for the entire processing (including the intermediate and final products generation) is 3.7 TB.

Among the instances available within the AWS EC2 platform, for our processing we selected the i3.16xlarge one [97] (Table III). This is highly performing in terms of available RAM and vCPUs and, most of all, it is equipped with internal SSD disks guaranteeing a very high input–output (I/O) bandwidth, which is essential when intensive I/O performances need to be sustained, as in the case of S-1 IW large data sets. We distributed the concurrent jobs of the P-SBAS processing among the available vCPUs by taking into account, for each parallel step of the workflow in Fig. 7, the maximum RAM

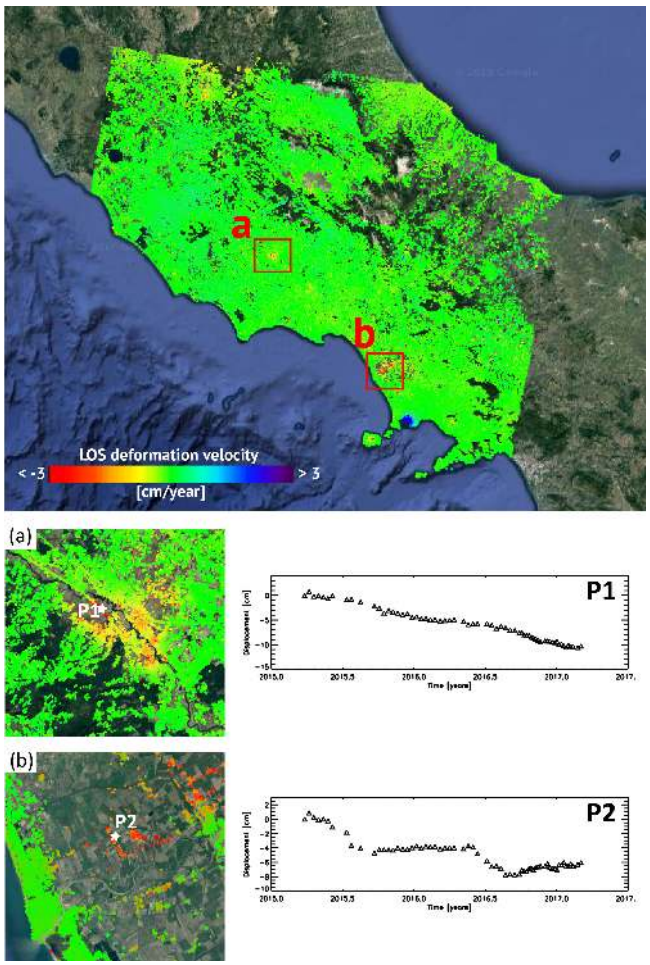

Fig. 16. Mean deformation velocity map relevant to the S-1 IW frame T22_N2 (see Fig. 8 and Table I), generated through the P-SBAS processing chain by exploiting the AWS EC2 CC resources described in Table III. The insets (a) and (b) show the zoomed-in views of two subsiding areas relevant to the high-speed railway and the Volturno River plain, respectively. The deformation time series of two pixels, labeled as P1 and P2, located in the corresponding maximum deformation areas are shown as well.

exploitation, the percentage of used CPU and the I/O load in order to optimize the exploitation of the resources, according to the strategy described in [76].

The elapsed time needed to transfer the S-1 IW input data from the S3 AWS archive to the EC2 instance was of approximately 1 hour while the time for the overall P-SBAS processing was equal to about 24.9 h; finally, the upload of the final P-SBAS results to the S3 storage took just a few minutes. Therefore, the overall processing took less than 30 h to run. In Table IV, we present the details of the elapsed processing times for each P-SBAS processing step depicted in Fig. 7, also specifying which are parallel or sequentially executed.

For the sake of completeness, we also present in Fig. 16 the mean deformation velocity map relevant to the selected S-1 IW frame, geocoded and superimposed on an optical image of the area of interest. Note that, due to the multilook operation performed on the interferograms, the final spacing of the map is of about 70×70 m^2. We remind that the estimated mean deformation velocity is only computed in coherent areas; accordingly, also in this case, the areas where the displacement accuracy is affected by significant decorrelation noise effects

TABLE IV
ELAPSED PROCESSING TIMES FOR EACH P-SBAS STEP DEPICTED IN FIG. 7

S-1 P-SBAS steps	Processing Time [min]
A (parallel on SLCs)	15
B (sequential)	39
C (parallel on bursts)*	8
D (parallel on bursts)	542
E (parallel on interferograms)	103
F (parallel on pixels)	154
G (sequential)	3
H (parallel on 3D stacks)	358
I (parallel on pixels)	273
Total	**1495 (24.9 hours)**

are excluded from the map. In Fig. 16(a) and (b), we also present the zoomed-in view of two areas which are particularly interesting from the deformation viewpoint, that are delineated in Fig. 16 by the red rectangles (a) and (b), respectively. In particular, in the inset 16(a) we show a zoomed in of the mean deformation velocity map over a stretch of the high-speed railway, where subsidence phenomena are evident; in this case we also present the plot of the computed deformation time series for one of the pixels characterized by the maximum deformation rate (P1), showing about 10 cm of cumulated displacement in the observed period. Moreover, in the inset 16(b) we depict a zoomed in of the mean deformation velocity map relevant to the subsidence effects characterizing Volturno River Plain; in this case the corresponding plot of the deformation time series of a selected pixel (P2) highlights the fluctuations superimposed on the long-term displacements due to the groundwater withdrawal.

VI. CONCLUSION

In this paper, we presented an efficient DInSAR processing chain based on the P-SBAS algorithm, for the generation of S-1 IW deformation time series. The developed processing chain fully benefits from the data acquisition characteristics of the S-1 IW mode and properly exploits efficient algorithms to automatically and effectively process large S-1 IW data sets. In addition, the original stripmap P-SBAS processing chain was enhanced with a further parallel granularity level that benefits from the burst partitioning, characterizing the S-1 IW data. The main algorithmic enhancements regard the accurate generation of burst interferograms, which needs a precise coregistration step and an appropriate burst interferograms correction to filter out unwanted azimuthal phase ramps related to possible residual azimuthal misregistration errors greater than 5×10^{-3} samples. Moreover, the presented P-SBAS processing chain is also suitable to be migrated on high-performance distributed computing infrastructures, such as CC environments.

An extensive experimental analysis was presented, based on the exploitation of a huge S-1 IW multitemporal data set, relevant to the overall Italian territory, consisting of thousands of slices acquired along descending orbits during the March 2015–April 2017 time interval. To assess the accuracy of the generated interferograms, we considered the final (phase corrected) differential interferograms and investigated the standard deviation values of the residual phase variations in the overlapping regions between the azimuth adjacent bursts. Our analysis reveals that only seven interferograms out of 7287 (less than 0.1%) show a standard deviation value greater than 5×10^{-3} samples, being the maximum computed value equal to 5.4×10^{-3} samples, thus clearly demonstrating the high accuracy of the achieved results. Moreover, in order to assess the quality of the deformation time series obtained by applying the developed S-1 IW P-SBAS processing chain, we presented a quantitative analysis based on the comparison of the achieved results with the measurements collected by hundreds of GPS stations (assumed as reference) deployed along the Italian territory. In this case, the performed analysis clearly reveals the capability of the implemented S-1 IW P-SBAS processing chain to retrieve displacement time series with sub-centimetric accuracy. In particular, the mean standard deviation value of the differences between the DInSAR and the LOS-projected GPS measurements is less than 0.5 cm. Moreover, a discussion about the performance achieved by migrating the developed processing chain within the AWS CC environment was presented, highlighting that a two-year data set relevant to a standard S-1 IW slice can be reliably processed in about 30 h.

These results demonstrate the capability of the P-SBAS approach to efficiently process large S-1 IW data sets to retrieve accurate displacement measurements of large portions of the Earth surface. This is particularly relevant in the light of the recent launch of the Copernicus Data and Information Access Services (DIAS), whose development has been carried out by the European Commission with the support of the European Space Agency [98]. This European initiative has the key objective to promote the joint exploitation of Copernicus data and CC services for entrepreneurs, scientists and public authorities, in order to favor the development of Copernicus-based services. Through the exploitation of the services made available by the DIAS providers and those relevant to advanced tools, such as the presented S-1 IW P-SBAS processing chain, the main task is to spread advanced satellite products to a wide user community. This goal is further fostered by the integration of automatic and effective satellite tools and services within national and transnational research infrastructures. In this context, a key role is represented by the European Plate Observing System (EPOS) [99], a long-term plan to facilitate the integrated use and reuse of data and products provided by European distributed research infrastructures for Solid Earth Science. Within EPOS, the satellite services based on the exploitation of advanced DInSAR tools will supply to the Solid Earth Science community products suitable to be used in several application scenarios, such as the study of the physical processes relevant to earthquakes, volcanic unrest episodes and eruptions, land motions and, more generally, to those driving the earth surface dynamics. With this respect, the presented S-1 IW P-SBAS processing chain can play a key role in generating updated information on the on-going surface deformation phenomena with an unprecedented spatial and temporal coverage.

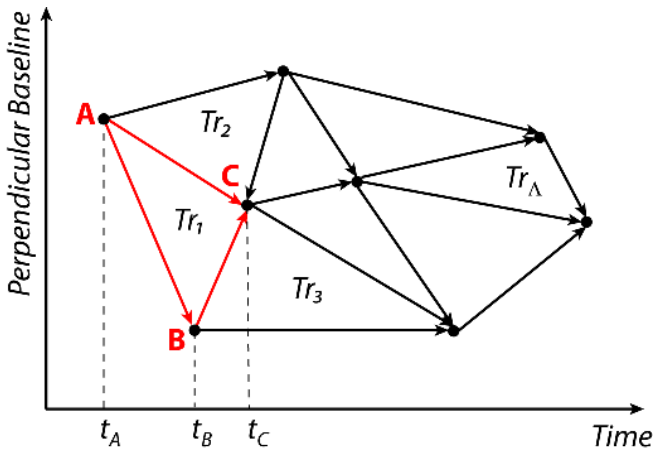

Fig. 17. Example of triangular network within the perpendicular-baseline/time interferometric plane; we highlight with the red color a single triangle.

APPENDIX

Let us focus on the issue of identifying the pixels to be investigated in the steps following the interferograms generation (such as the PhU and the deformation time series retrieval), within the developed advanced DInSAR processing chain. To achieve this task, an effective solution relies on the observation that the wrapped sum of three generic multilook interferograms forming a triangle in the perpendicular baseline/time plane (see Fig. 17) is, for each pixel, typically different from zero because it accounts for the time-inconsistent phase noise components of the considered interferograms triples [11], [74], [78], [100]. Indeed, the wrapped sum for each pixel of three generic interferograms, namely $\Delta\phi_{BA} = Wr(\phi_B - \phi_A)$, $\Delta\phi_{CB} = Wr(\phi_C - \phi_B)$, and $\Delta\phi_{AC} = Wr(\phi_A - \phi_C)$, computed from the SAR data acquired at the different times t_A, t_B and t_C (see the red triangle in Fig. 17) turns out to be different from zero [11], [74], [78], [100]

$$Wr[\Delta\phi_{BA} + \Delta\phi_{CB} + \Delta\phi_{AC}] = \Delta\phi_{\text{res}} \neq 0, \qquad \text{(A1)}$$

being Wr $[\cdot]$ the wrapping operator.

We further remark that this property is still valid for the sequence of noise-filtered DInSAR interferograms obtained by applying the procedure described in [74]. Note also that in the developed processing chain we implement a selection, among all the exploited interferometric data pairs, of an optimized triangular network within the perpendicular-baseline/time plane [75]. This triangulation is composed of Λ triangles and M^{tr} arcs, the latter corresponding to the selected SB interferometric pairs. Accordingly, for each triangle and each pixel P of the azimuth/range spatial domain, we can compute the residual phases, say $\Delta\phi^{tr}_{\text{res}_i}(P), i = 1, \ldots, \Lambda$ by considering (A1). As mentioned above these phase residuals get indirect information on the presence of

uncompensated noise phase signals in the involved interferograms. Accordingly, the coherent pixels to be analyzed through the developed processing chain can be efficiently selected by computing, on a pixel-by-pixel basis, the values of an equivalent coherence factor [100], which is referred hereinafter as triangular coherence and is defined as follows:

$$\Upsilon(P) = \frac{1}{\Lambda}\left|\sum_{k=1}^{\Lambda}\exp\left[j\,\Delta\phi_{\mathrm{res}_k}^{tr}(P)\right]\right| \in [0,\,1]. \qquad \text{(A2)}$$

Pixels with high values (greater than a selected threshold, say γ) of the triangular coherence correspond to the sparse grid of data, namely S, over which the subsequent PhU operation is carried out, that is: $S = \{P : \Upsilon(P) \geq \gamma\}$.

Tests performed on several case studies revealed that suitable values of the threshold γ are typically within the [0.7, 0.9] range.

ACKNOWLEDGMENT

The Digital Elevation Models of the analyzed areas were acquired through the SRTM archive. This paper contains modified Copernicus Sentinel data (2019).

REFERENCES

[1] R. Bürgmann, P. A. Rosen, and E. J. Fielding, "Synthetic aperture radar interferometry to measure Earth's surface topography and its deformation," *Annu. Rev. Earth Planet. Sci.*, vol. 28, no. 1, pp. 169–209, 2000.

[2] D. Massonnet and K. L. Feigl, "Radar interferometry and its application to changes in the Earth's surface," *Rev. Geophys.*, vol. 36, no. 4, pp. 441–500, Nov. 1998.

[3] A. K. Gabriel, R. M. Goldstein, and H. A. Zebker, "Mapping small elevation changes over large areas: Differential interferometry," *J. Geophys. Res.*, vol. 94, no. B7, pp. 9183–9191, 1989.

[4] R. M. Goldstein, H. A. Zebker, and C. L. Werner, "Satellite radar interferometry: Two-dimensional phase unwrapping," *Radio Sci.*, vol. 23, no. 4, pp. 713–720, Aug. 1988.

[5] G. Franceschetti and R. Lanari, *Synthetic Aperture Radar Processing*. Boca Raton, FL, USA: CRC Press, 1999.

[6] P. A. Rosen *et al.*, "Synthetic aperture radar interferometry," *Proc. IEEE*, vol. 88, no. 3, pp. 333–382, Mar. 2000.

[7] D. Massonnet *et al.*, "The displacement field of the Landers earthquake mapped by radar interferometry," *Nature*, vol. 364, no. 6433, pp. 138–142, 1993.

[8] P. Berardino, G. Fornaro, R. Lanari, and E. Sansosti, "A new algorithm for surface deformation monitoring based on small baseline differential SAR interferograms," *IEEE Trans. Geosci. Remote Sens.*, vol. 40, no. 11, pp. 2375–2383, Nov. 2002.

[9] M. Crosetto, B. Crippa, and E. Biescas, "Early detection and in-depth analysis of deformation phenomena by radar interferometry," *Eng. Geol.*, vol. 79, pp. 81–91, Jun. 2005.

[10] A. Ferretti, C. Prati, and F. Rocca, "Permanent scatterers in SAR interferometry," *IEEE Trans. Geosci. Remote Sens.*, vol. 39, no. 1, pp. 8–20, Jan. 2001.

[11] A. Ferretti, A. Fumagalli, F. Novali, C. Prati, F. Rocca, and A. Rucci, "A new algorithm for processing interferometric data-stacks: SqueeSAR," *IEEE Trans. Geosci. Remote Sens.*, vol. 49, no. 9, pp. 3460–3470, Sep. 2011.

[12] A. Hooper, "A multi-temporal InSAR method incorporating both persistent scatterer and small baseline approaches," *Geophys. Res. Lett.*, vol. 35, no. 16, pp. L16–L302, 2008.

[13] B. M. Kampes, *Radar Interferometry: Persistent Scatterer Technique*. Dordrecht, The Netherlands: Springer, 2006.

[14] R. Lanari, O. Mora, M. Manunta, J. J. Mallorquí, P. Berardino, and E. Sansosti, "A small-baseline approach for investigating deformations on full-resolution differential SAR interferograms," *IEEE Trans. Geosci. Remote Sens.*, vol. 42, no. 7, pp. 1377–1386, Jul. 2004.

[15] O. Mora, J. J. Mallorqui, and A. Broquetas, "Linear and nonlinear terrain deformation maps from a reduced set of interferometric SAR images," *IEEE Trans. Geosci. Remote Sens.*, vol. 41, no. 10, pp. 2243–2253, Oct. 2003.

[16] C. Werner, U. Wegmuller, T. Strozzi, and A. Wiesmann, "Interferometric point target analysis for deformation mapping," in *Proc. Geosci. Remote Sens. Symp.*, Toulouse, France, vol. 7, 2003, pp. 4362–4364.

[17] E. Sansosti, F. Casu, M. Manzo, and R. Lanari, "Space-borne radar interferometry techniques for the generation of deformation time series: An advanced tool for Earth's surface displacement analysis," *Geophys. Res. Lett.*, vol. 37, Oct. 2010, Art. no. L20305. doi: 10.1029/2010GL044379.

[18] F. Casu, M. Manzo, and R. Lanari, "A quantitative assessment of the SBAS algorithm performance for surface deformation retrieval from DInSAR data," *Remote Sens. Environ.*, vol. 102, nos. 3–4, pp. 195–210, Jun. 2006.

[19] M. Bonano, M. Manunta, A. Pepe, L. Paglia, and R. Lanari, "From previous C-band to new X-band SAR systems: Assessment of the DInSAR mapping improvement for deformation time-series retrieval in urban areas," *IEEE Trans. Geosci. Remote Sens.*, vol. 51, no. 4, pp. 1973–1984, Apr. 2013.

[20] M. Manunta, M. Marsella, G. Zeni, M. Sciotti, S. Atzori, and R. Lanari, "Two-scale surface deformation analysis using the SBAS-DInSAR technique: A case study of the city of Rome, Italy," *Int. J. Remote Sens.*, vol. 29, no. 6, pp. 1665–1684, 2008.

[21] A. Pepe, E. Sansosti, P. Berardino, and R. Lanari, "On the generation of ERS/ENVISAT DInSAR time-series via the SBAS technique," *IEEE Geosci. Remote Sens Lett.*, vol. 2, no. 3, pp. 265–269, Jul. 2005.

[22] M. Bonano, M. Manunta, M. Marsella, and R. Lanari, "Long-term ERS/ENVISAT deformation time-series generation at full spatial resolution via the extended SBAS technique," *Int. J. Remote Sens.*, vol. 33, pp. 4756–4783, Aug. 2012.

[23] H. A. Zebker and J. Villasenor, "Decorrelation in interferometric radar echoes," *IEEE Trans. Geosci. Remote Sens.*, vol. 30, no. 5, pp. 950–959, Sep. 1992.

[24] R. Lanari *et al.*, "Evidence for a peculiar style of ground deformation inferred at Vesuvius volcano," *Geophys. Res. Lett.*, vol. 29, no. 9, pp. 6-1–6-4, 2002. doi: 10.1029/2001GL014571.

[25] J. Fernández *et al.*, "Gravity-driven deformation of Tenerife measured by InSAR time series analysis," *Geophys. Res. Lett.*, vol. 36, no. 4, 2009, Art. no. L04306. doi: 10.1029/2008GL036920.

[26] J. Ruch *et al.*, "Stress transfer in the Lazufre volcanic area, central Andes," *Geophys. Res. Lett.*, vol. 36, no. 22, 2009, Art. no. L22303. doi: 10.1029/2009GL041276.

[27] A. Manconi *et al.*, "On the effects of 3-D mechanical heterogeneities at Campi Flegrei caldera, southern Italy," *J. Geophys. Res., Space Phys.*, vol. 115, no. 8, 2010, Art. no. B08405. doi: 10.1029/2009JB007099.

[28] I. Hunstad, A. Pepe, S. Atzori, C. Tolomei, S. Salvi, and R. Lanari, "Surface deformation in the Abruzzi region, Central Italy, from multitemporal DInSAR analysis," *Geophys. J. Int.*, vol. 178, no. 3, pp. 1193–1197, 2009. doi: 10.1111/j.1365-246X.2009.04284.x.

[29] R. Lanari *et al.*, "Surface displacements associated with the L'Aquila 2009 Mw 6.3 earthquake (central Italy): New evidence from SBAS-DInSAR time series analysis," *Geophys. Res. Lett.*, vol. 37, no. 20, 2010, Art. no. L20309. doi: 101029/2010GL044780.

[30] M. Manzo, Y. Fialko, F. Casu, A. Pepe, and R. Lanari, "A quantitative assessment of DInSAR measurements of interseismic deformation: The Southern San Andreas fault case study," *Pure Appl. Geophys.*, vol. 169, no. 8, pp. 1463–1482, 2011. doi: 10.1007/s00024-011-0403-2.

[31] F. Diao *et al.*, "Fault locking near Istanbul: indication of earthquake potential from InSAR and GPS observations," *Geophys. J. Int.*, vol. 205, pp. 490–498, Feb. 2016.

[32] L. Cascini, S. Ferlisi, G. Fornaro, R. Lanari, D. Peduto, and G. Zeni, "Subsidence monitoring in Sarno urban area via multitemporal DInSAR technique," *Int. J. Remote Sens.*, vol. 27, no. 8, pp. 1709–1716, 2006.

[33] A. Perrone *et al.*, "Joint analysis of SAR interferometry and electrical resistivity tomography surveys for investigating ground deformation: The case-study of Satriano di Lucania (Potenza, Italy)," *Eng. Geol.*, vol. 88, pp. 260–273, Dec. 2006.

[34] F. Calò *et al.*, "Enhanced landslide investigations through advanced DInSAR techniques: The Ivancich case study, Assisi, Italy," *Remote Sens. Environ.*, vol. 142, pp. 69–82, Feb. 2014.

[35] R. Lanari, G. Zeni, M. Manunta, S. Guarino, P. Berardino, and E. Sansosti, "An integrated SAR/GIS approach for investigating urban deformation phenomena: A case study of the city of Naples, Italy," *Int. J. Remote Sens.*, vol. 25, pp. 2855–2867, Jul. 2004.

[36] G. Zeni *et al.*, "Long-term deformation analysis of historical buildings through the advanced SBAS-DInSAR technique: The case study of the city of Rome, Italy," *J. Geophys. Eng.*, vol. 8, no. 3, pp. S1–S12, 2011.

[37] M. Bonano, M. Manzo, F. Casu, M. Manunta, and R. Lanari, "DInSAR for the monitoring of cultural heritage sites," in *Sensing the Past* (Geotechnologies and the Environment), N. Masini and F. Soldovieri, Eds. Cham, Switzerland: Springer, 2016, ch. 6, pp. 117–134.

[38] S. Scifoni *et al.*, "On the joint exploitation of long-term DInSAR time series and geological information for the investigation of ground settlements in the town of Roma (Italy)," *Remote Sens. Environ.*, vol. 182, pp. 113–127, Sep. 2016.

[39] L. Solari *et al.*, "Combined use of C-and X-Band SAR data for subsidence monitoring in an urban area," *Geosciences*, vol. 7, no. 2, p. 21, 2017. doi: 10.3390/geosciences7020021.

[40] Q. Zhao *et al.*, "A DInSAR investigation of the ground settlement time evolution of ocean-reclaimed lands in Shanghai," *IEEE J. Sel. Topics Appl. Earth Observ. Remote Sens.*, vol. 8, no. 4, pp. 1763–1781, Apr. 2015. doi: 10.1109/JSTARS.2015.240216.

[41] D. Notti *et al.*, "A user-oriented methodology for DInSAR time series analysis and interpretation: Landslides and subsidence case studies," *Pure Appl. Geophys.*, vol. 172, no. 11, pp. 3081–3105, Mar. 2015.

[42] F. Casu *et al.*, "SBAS-DInSAR parallel processing for deformation time-series computation," *IEEE J. Sel. Top. Appl. Earth Observ. Remote Sens.*, vol. 7, no. 8, pp. 3285–3296, Aug. 2014.

[43] I. Zinno *et al.*, "A first assessment of the P-SBAS DInSAR algorithm performances within a cloud computing environment," *IEEE J. Sel. Topics Appl. Earth Observ. Remote Sens.*, vol. 8, no. 10, pp. 4675–4686, Oct. 2015.

[44] I. Zinno *et al.*, "Cloud computing for Earth surface deformation analysis via spaceborne radar imaging: A case study," *IEEE Trans. Cloud Comput.*, vol. 4, no. 1, pp. 104–118, Jan. 2016.

[45] I. Zinno, F. Casu, C. D. Luca, S. Elefante, R. Lanari, and M. Manunta, "A cloud computing solution for the efficient implementation of the P-SBAS DInSAR approach," *IEEE J. Sel. Topics Appl. Earth Observ. Remote Sens.*, vol. 10, no. 3, pp. 802–817, Mar. 2017.

[46] R. Torres, S. Løkås, D. Geudtner, and B. Rosich, "Sentinel-1A LEOP and commissioning," in *Proc. IEEE IGARSS*, Quebec City, QC, Canada, Jul. 2014, pp. 1469–1472. doi: 10.1109/IGARSS.2014.6946714.

[47] N. Yagüe-Martínez *et al.*, "Interferometric processing of Sentinel-1 TOPS data," *IEEE Trans. Geosci. Remote Sens.*, vol. 54, no. 4, pp. 2220–2234, Apr. 2016.

[48] R. Torres *et al.*, "GMES Sentinel-1 mission," *Remote Sens. Environ.*, vol. 120, pp. 9–24, May 2012.

[49] N. Miranda *et al.*, "Sentinel-1B preliminary results obtained during the orbit acquisition phase [work in progress]," *Procedia Comput. Sci.*, vol. 100, pp. 1313–1318, Jan. 2016.

[50] C. De Luca *et al.*, "An on-demand Web tool for the unsupervised retrieval of Earth's surface deformation from SAR data: The P-SBAS service within the ESA G-POD environment," *Remote Sens.*, vol. 7, no. 11, pp. 15630–15650, 2015. doi: 10.3390/rs71115630.

[51] *The Geohazard Exploitation Platform and Portal*. Accessed: Apr. 25, 2019. [Online]. Available: https://geohazards-tep.eo.esa.int/#!pages/initiative

[52] F. De Zan and A. M. Guarnieri, "TOPSAR: Terrain observation by progressive scans," *IEEE Trans. Geosci. Remote Sens.*, vol. 44, no. 9, pp. 2352–2360, Sep. 2006.

[53] P. Prats-Iraola, R. Scheiber, L. Marotti, S. Wollstadt, and A. Reigber, "TOPS interferometry with TerraSAR-X," *IEEE Trans. Geosci. Remote Sens.*, vol. 50, no. 8, pp. 3179–3188, Aug. 2012.

[54] K. Dai *et al.*, "Monitoring activity at the Daguangbao mega-landslide (China) using Sentinel-1 TOPS time series interferometry," *Remote Sens. Environ.*, vol. 186, pp. 501–513, Dec. 2016.

[55] U. Wegmüller, C. Werner, T. Strozzi, A. Wiesmann, O. Frey, and M. Santoro, "Sentinel-1 support in the GAMMA software," *Procedia Comput. Sci.*, vol. 100, pp. 1305–1312, Jan. 2016.

[56] Y. Qin, D. Perissin, and J. Bai, "A common 'stripmap-like' interferometric processing chain for TOPS and ScanSAR wide swath mode," *Remote Sens.*, vol. 10, no. 10, p. 1504, 2018.

[57] M. Nannini, P. Prats-Iraola, Z. F. De, and D. Geudtner, "TOPS time series performance assessment with TerraSAR-X data," *IEEE J. Sel. Topics Appl. Earth Observ. Remote Sens.*, vol. 9, no. 8, pp. 3832–3848, Aug. 2016.

[58] D. Sandwell, R. Mellors, X. Tong, M. Wei, and P. Wessel, "Open radar interferometry software for mapping surface deformation," *EOS, Trans. Amer. Geophys. Union*, vol. 92, no. 28, p. 234, 2011. doi: 10.1029/2011EO280002.

[59] *The InSAR Scientific Computing Environment (ISCE) Software*. Accessed: Apr. 25, 2019. [Online]. Available: https://winsar.unavco.org/software/isce

[60] R. Scheiber and A. Moreira, "Coregistration of interferometric SAR images using spectral diversity," *IEEE Trans. Geosci. Remote Sens.*, vol. 38, no. 5, pp. 2179–2191, Sep. 2000.

[61] N. Yague-Martinez, F. De Zan, and P. Prats-Iraola, "Coregistration of interferometric stacks of Sentinel-1 TOPS data," *IEEE Geosci. Remote Sens. Lett.*, vol. 14, no. 7, pp. 1002–1006, Jul. 2017. doi: 10.1109/LGRS.2017.2691398.

[62] A. Ferretti, D. Colombo, A. Fumagalli, F. Novali, and A. Rucci, "InSAR data for monitoring land subsidence: Time to think big," *Proc. Int. Assoc. Hydrol. Sci.*, vol. 372, pp. 331–334, Nov. 2015.

[63] (2015). *Amazon Web Services (AWS)*. [Online]. Available: https://aws.amazon.com/

[64] C. De Luca, I. Zinno, M. Manunta, R. Lanari, and F. Casu, "Large areas surface deformation analysis through a cloud computing P-SBAS approach for massive processing of DInSAR time series," *Remote Sens. Environ.*, vol. 202, pp. 3–17, Dec. 2017.

[65] K. Tomiyasu, "Conceptual performance of a satellite borne, wide swath synthetic aperture radar," *IEEE Trans. Geosci. Remote Sens.*, vol. 19, no. 2, pp. 108–116, Apr. 1981.

[66] P. J. González *et al.*, "The 2014–2015 eruption of Fogo volcano: Geodetic modeling of Sentinel-1 TOPS interferometry," *Geophys. Res. Lett.*, vol. 42, pp. 9239–9246, Nov. 2015. doi: 10.1002/2015GL066003.

[67] G. Solaro *et al.*, "Coseismic fault model of Mw 8.3 2015 Illapel earthquake (Chile) retrieved from multi-orbit Sentinel1-A DInSAR measurements," *Remote Sens.*, vol. 8, no. 4, p. 323, 2016.

[68] G. Lavecchia *et al.*, "Ground deformation and source geometry of the 24 August 2016 Amatrice earthquake (Central Italy) investigated through analytical and numerical modeling of DInSAR measurements and structural-geological data," *Geophys. Res. Lett.*, vol. 43, no. 12, pp. 389–398, 2016. doi: 10.1002/2016GL071723.

[69] D. Cheloni *et al.*, "Geodetic model of the 2016 Central Italy earthquake sequence inferred from InSAR and GPS data," *Geophys. Res. Lett.*, vol. 44, no. 13, pp. 6778–6787, 2017.

[70] E. Sansosti, P. Berardino, M. Manunta, F. Serafino, and G. Fornaro, "Geometrical SAR image registration," *IEEE Trans. Geosci. Remote Sens.*, vol. 44, no. 10, pp. 2861–2870, Oct. 2006.

[71] R. Lanari *et al.*, "Sentinel-1 results: SBAS-DInSAR processing chain developments and land subsidence analysis," in *Proc. IEEE Int. Geosci. Remote Sens. Symp.*, Jul. 2015, pp. 2836–2839.

[72] H. Fattahi, P. Agram, and M. Simons, "A network-based enhanced spectral diversity approach for TOPS time-series analysis," *IEEE Trans. Geosci. Remote Sens.*, vol. 55, no. 2, pp. 777–786, Feb. 2017.

[73] M. Cignetti *et al.*, "Taking advantage of the ESA G-POD service to study ground deformation processes in high mountain areas: A Valle d'Aosta case study, Northern Italy," *Remote Sens.*, vol. 8, no. 10, p. 852, 2016. doi: 10.3390/rs8100852.

[74] A. Pepe, Y. Yang, M. Manzo, and R. Lanari, "Improved EMCF-SBAS processing chain based on advanced techniques for the noise-filtering and selection of small baseline multi-look DInSAR interferograms," *IEEE Trans. Geosci. Remote Sens.*, vol. 53, no. 8, pp. 4394–4417, Aug. 2015.

[75] Y. Yang, A. Pepe, M. Manzo, M. Bonano, D. N. Liang, and R. Lanari, "A simple solution to mitigate noise effects in time-redundant sequences of small baseline multi-look DInSAR interferograms," *Remote Sens. Lett.*, vol. 4, no. 6, pp. 609–618, 2013.

[76] I. Zinno *et al.*, "National scale surface deformation time series generation through advanced DInSAR processing of sentinel-1 data within a cloud computing environment," *IEEE Trans. Big Data*, to be published. doi: 10.1109/TBDATA.2018.2863558.

[77] J. C. Curlander and R. McDonough, *Synthetic Aperture Radar: System and Signal Processing*. New York, NY, USA: Wiley, 1991.

[78] A. Pepe and R. Lanari, "On the extension of the minimum cost flow algorithm for phase unwrapping of multitemporal differential SAR interferograms," *IEEE Trans. Geosci. Remote Sens.*, vol. 44, no. 9, pp. 2374–2383, Sep. 2006.

[79] P. Imperatore, A. Pepe, and R. Lanari, "Multichannel phase unwrapping: Problem topology and dual-level parallel computational model," *IEEE Trans. Geosci. Remote Sens.*, vol. 53, no. 10, pp. 5774–5793, Oct. 2015.

[80] C. Liang, E. J. Fielding, and M. H. Huang, "Estimating azimuth offset with double-difference interferometric phase: The effect of azimuth FM rate error in focusing," *IEEE Trans. Geosci. Remote Sens.*, vol. 55, no. 12, pp. 7018–7031, Dec. 2017.

[81] D. Colombo, P. Farina, S. Moretti, G. Nico, and C. Prati, "Land subsidence in the Firenze-Prato-Pistoia basin measured by means of spaceborne SAR interferometry," in *Proc. IGARSS*, Jul. 2003, pp. 2927–2929.
[82] F. Raspini *et al.*, "Advanced interpretation of interferometric SAR data to detect, monitor and model ground subsidence: Outcomes from the ESA-GMES Terrafirma project," *Natural Hazards*, vol. 83, no. 1, pp. 155–181, 2016. doi: 10.1007/s11069-016-2341-x.
[83] R. Lanari *et al.*, "An overview of the Small BAseline Subset algorithm: A DInSAR technique for surface deformation analysis," *Pure Appl. Geophys.*, vol. 164, no. 4, pp. 637–661, 2007.
[84] E. Trasatti *et al.*, "The 2004–2006 uplift episode at Campi Flegrei Caldera (Italy): Constraints from SBAS-DInSAR ENVISAT data and Bayesian source inference," *Geophys. Res. Lett.*, vol. 35, no. 7, 2008, Art. no. L073078. doi: 10.1029/2007GL033091.
[85] L. D'Auria, F. Giudicepietro, M. Martini, and R. Lanari, "The 4D imaging of the source of ground deformation at Campi Flegrei caldera (southern Italy)," *J. Geophys. Res., Solid Earth*, vol. 117, Aug. 2012, Art. no. B08209. doi: 10.1029/2012JB009181.
[86] A. Amoruso, L. Crescentini, and I. Sabbetta, "Paired deformation sources of the Campi Flegrei caldera (Italy) required by recent (1980–2010) deformation history," *J. Geophys. Res., Solid Earth*, vol. 119, pp. 858–879, Feb. 2014. doi: 10.1002/2013JB010392.
[87] A. Amoruso, L. Crescentini, I. Sabbetta, P. De Martino, F. Obrizzo, and U. Tammaro, "Clues to the cause of the 2011–2013 Campi Flegrei caldera unrest, Italy, from continuous GPS data," *Geophys. Res. Lett.*, vol. 41, no. 9, pp. 3081–3088, 2014. doi: 10.1002/2014GL059539.
[88] L. D'Auria *et al.*, "Magma injection beneath the urban area of Naples: A new mechanism for the 2012–2013 volcanic unrest at Campi Flegrei caldera," *Sci. Rep.*, vol. 5, Aug. 2015, Art. no. 13100. doi: 10.1038/srep13100.
[89] G. Iannaccone *et al.*, "Measurement of seafloor deformation in the marine sector of the Campi Flegrei caldera (Italy)," *J. Geophys. Res., Solid Earth*, vol. 123, pp. 66–83, Jan. 2018. [Online]. Available: https://doi.org/10.1002/2017JB014852
[90] P. De Martino, U. Tammaro, and F. Obrizzo, "GPS time series at Campi Flegrei caldera (2000-2013)," *Ann. Geophys.*, vol. 57, no. 2, 2014, Art. no. S0213. doi: 10.4401/ag-6431S0213.
[91] U. Tammaro *et al.*, "Somma Vesuvius volcano: Ground deformations from CGPS observations (2001-2012)," *Ann. Geophys.*, vol. 56, no. 4, 2013, Art. no. S0456. doi: 10.4401/ag-6462.
[92] G. Blewitt, W. C. Hammond, and C. Kreemer, "Harnessing the GPS data explosion for interdisciplinary science," *Eos*, vol. 99, Sep. 2018. doi: 10.1029/2018EO104623.
[93] *InSAR Processing Tools on AWS*. Accessed: Apr. 25, 2019. [Online]. Available: https://github.com/scottyhq/dinosar
[94] *Amazon EC2*. Accessed: Apr. 25, 2019. [Online]. Available: http://docs.aws.amazon.com/AWSEC2/latest/UserGuide/concepts.html
[95] *Amazon Storage*. Accessed: Apr. 25, 2019. [Online]. Available: https://docs.aws.amazon.com/AWSEC2/latest/UserGuide/Storage.html
[96] *Copernicus Open Access Hub*. Accessed: Apr. 25, 2019. [Online]. Available: https://scihub.copernicus.eu
[97] *i3.16xlarge AWS Instance*. Accessed: Apr. 25, 2019. [Online]. Available: https://aws.amazon.com/it/ec2/instance-types/
[98] *Copernicus Data and Information Access Services (DIAS)*. Accessed: Apr. 25, 2019. [Online]. Available: http://copernicus.eu/news/upcoming-copernicus-data-and-information-access-services-dias
[99] *European Plate Observing System (EPOS)*. Accessed: Apr. 25, 2019. [Online]. Available: https://www.epos-ip.org
[100] A. Pepe, *Advanced Differential Interferometric SAR Techniques: The Extended Minimum Cost Flow Phase Unwrapping (EMCF) Technique*. Saarbrucken, Germany: VDM Verlang, 2009.

Michele Manunta was born in Cagliari, Italy, in 1975. He received the Laurea degree in electronic engineering and the Ph.D. degree in informatics and electronic engineering from the University of Cagliari, Cagliari, Italy, in 2001 and 2009, respectively.

Since 2002, he has been with the Istituto per il Rilevamento Elettromagnetico dell'Ambiente, Italian National Research Council (CNR), Naples, Italy, where he is currently a Researcher. He was a Visiting Scientific with the Institut Cartografic de Catalunya, Barcelona, Spain, in 2004, and the Rosenstiel School of Marine and Atmospheric Science, University of Miami, Coral Gables, FL, USA, in 2006. He has been contributing in various national and international initiatives for the exploitation of satellite technologies, and in particular of SAR techniques. He is coordinating the satellite component of the EPOS research infrastructure. His research interests include high-resolution synthetic aperture radar (SAR), differential SAR interferometry (DInSAR) data processing and application, the development of SAR/DInSAR algorithms and techniques for studying deformation affecting terrain surface and man-made structures, and cloud and grid computing exploitation for SAR interferometry applications.

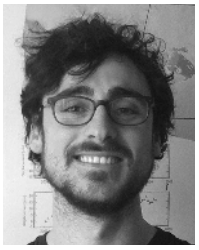

Claudio De Luca was born in Naples, Italy, in 1987. He received the Laurea degree (110/110) in telecommunication engineering from the University of Naples "Federico II," Naples, in 2012, and the Ph.D. degree in computer and automatic engineering with the Department of Electrical Engineering and Information Technology, University of Naples "Federico II," in 2016.

Since 2013, he has been a Research Fellow at the Istituto per il Rilevamento Elettromagnetico dell'Ambiente, National Research Council, Naples, mainly focusing on the development of advanced differential synthetic aperture radar (SAR) interferometry (InSAR) techniques for deformation time-series generation by also exploiting parallel computing platforms. His research interests include cloud computing solution for intensive processing of remote sensing data, and the development of advanced algorithm for Sentinel-1 SAR and InSAR data processing.

Ivana Zinno was born in Naples, Italy, in 1980. She received the Laurea degree (*summa cum laude*) in telecommunication engineering and the Ph.D. degree in electronic and telecommunication engineering from the University of Naples Federico II, Naples, in 2008 and 2011, respectively.

In 2011, she received a grant from the University of Naples to be spent at the Department of Electronic and Telecommunication Engineering for research in the field of remote sensing. Since 2012, she has been with the IREA-National Research Council, Naples, where she is currently a Researcher. In 2017, she has been a Visiting Scientist with the Jet Propulsion Laboratory, Pasadena, CA, USA. She currently focuses on the development of advanced differential synthetic aperture radar (SAR) interferometry (DInSAR) techniques for surface deformation time series generation and on the exploitation of distributed computing architectures (grid and cloud computing platforms) for big SAR data processing. Her research interests include microwave remote sensing; in particular they concern DInSAR applications, with particular emphasis on novel generation satellite constellations such as Sentinel-1, and, more generally, the information retrieval from SAR data by also exploiting fractal models.

Francesco Casu received the Laurea degree (*summa cum laude*) and the Ph.D. degree in electronic engineering from the University of Cagliari, Cagliari, Italy, in 2003 and 2009, respectively.

Since 2003, he has been with IREA-CNR, Naples, Italy, where he is currently a permanent Researcher. He was a Visiting Scientist with the University of Texas at Austin, Austin, TX, USA, in 2004, the Jet Propulsion Laboratory, Pasadena, CA, USA, in 2005, and the Department of Geophysics, Stanford University, Stanford, CA, USA, in 2009. He is the scientific responsible of the IREA-CNR activities as Center of Competence of the Italian Civil Protection Department. More recently, he has been involved in the development of Differential synthetic aperture radar Interferometry (DInSAR) algorithms for unsupervised processing of huge SAR data archives by exploiting high-performance computing platforms, such as grid and cloud computing ones. His research interests include the DInSAR field, in the multipass interferometry [particularly concerning the improvement of the Small BAseline Subset (SBAS)-DInSAR algorithm] and in the SBAS-DInSAR measurement assessment, with a particular emphasis on novel generation satellite constellations such as COSMO-SkyMed, TerraSAR-X, and Sentinel-1.

Dr. Casu is a reviewer for several peer-reviewed international journals and he has served as a Scientific Committee Member of a number of international conferences.

Mariarosaria Manzo, was born in Naples, Italy, in 1973. She received the Laurea degree *(summa cum laude)* in mathematics from the University of Naples Federico II, Naples, in 1998, and the Ph.D. degree in methods and technologies for environmental monitoring from the University of Basilicata, Potenza, Italy, in 2008.

She joined the Istituto Per II Rilevamento Elettromagnetico Dell'Ambiente (IREA), Italian National Research Council (CNR), Naples, in 2002, where she is currently a permanent Researcher. She was a Visiting Researcher with the German Aerospace Center (DLR), Oberpfaffenhofen, Germany, in 2004, and the Geodesy Laboratory, University of Miami, Coral Gables, FL, USA, in 2007. She has been involved in several national and international research projects. She is also currently involved in several national and international research projects. Her current research interests include differential SAR interferometry (DInSAR), particularly, the development of algorithms for the generation of velocity maps and corresponding time series starting from SAR data acquired by the first- and second-generation satellite sensors, the applications of such algorithms for the monitoring of surface displacements, such as those produced by subsidence, volcano activity, earthquakes, and landslides, and the development of optimization/inversion algorithms for the analytical modeling of seismic and volcanic sources by using DInSAR and geodetic data.

Manuela Bonano received the Laurea degree (*summa cum laude*) in environmental engineering from the University of Cagliari, Cagliari, Italy, in 2004, and the Ph.D. degree in infrastructures and transportation from the University of Roma "La Sapienza," Rome, Italy, in 2012.

In 2007, she started her research activity in the SAR interferometry field at IREA-CNR, Naples, Italy, where she mainly focused on the development of advanced multipass interferometry algorithms for full resolution differential Synthetic aperture radar (SAR) interferometry (DInSAR) analyses of local deformation affecting single buildings and man-made structures. In 2011, she joined the Earth and Planetary Science Department, University of California at Berkeley, Berkeley, CA, USA, as a Visiting Scientist. Recently, she has been involved in the development of advanced DInSAR techniques for processing SAR data acquired by novel generation satellites, such as COSMO-SkyMed, TerraSAR-X, and Sentinel-1, based on the exploitation of advanced distributed computing technologies (HPC and GPU) and infrastructures (grid and cloud computing).

Adele Fusco received the Laurea degree (*cum laude*) in telecommunications engineering from the University of Naples, Naples, Italy, in 2000, and the Ph.D. degree in information engineering from the University of Sannio, Benevento, Italy, in 2004. Her Ph.D. thesis, done in collaboration with the Deutsches Zentrum fuer Luft und Raumfahrt (DLR), Oberphaffenhofen, Germany, focused on synthetic aperture radar interferometry.

From 2004 to 2012, she was with the Mediterranean Agency for Remote Sensing and Environmental Control, Benevento, as a Leading Expert in synthetic aperture radar data processing, a Technical Manager of the local satellite ground station, and a Coordinator of several national and international projects. Since 2013, she has been involved in the activity of The Waves Group at the University of Sannio, focusing on compressed sensing techniques for analyzing transient noise in interferometric detectors of gravitational waves and in connection with the LIGO, Virgo, and KAGRA collaborations. Since 2014, she has been a Research Fellow at CNR-IREA, Naples, developing efficient algorithms to process interferometric data from advanced satellite-borne synthetic aperture radars.

Antonio Pepe (M'12–SM'17) received the Laurea degree in electronic engineering and the Ph.D. degree in electronic and telecommunication engineering from the University of Naples Federico II, Naples, Italy, in 2000 and 2007, respectively.

After graduation, following a short experience at Wind Telecommunication S.p.a, Rome, Italy, he joined the Istituto per il Rilevamento Elettromagnetico dell'Ambiente, Italian National Research Council, Naples, in 2001, where he is currently a permanent Researcher. He was a Visiting Scientist at the University of Texas at Austin, Austin, TX, USA, in 2005, and at the Jet Propulsion Laboratory, Pasadena, CA, USA, in 2009, and he was A Foreigner Expert at the East China Normal University, Shanghai, China. Since 2012, he has also been an Adjunct Professor of signal theory and random signal theory with the Università della Basilicata, Potenza, Italy. More recently, he has developed research activities for the generation of differential synthetic aperture radar interferometry (DInSAR) products through the new generation SAR instruments, for the generation of hybrid scanSAR-to-stripmap DInSAR analyses, for the combination of DInSAR multisatellite data, for the filtering of sequences of multitemporal interferograms and for the integration of SAR and optical products. His research interests include the development of advanced DInSAR algorithms aimed at monitoring surface deformation phenomena induced by subsidence, volcano activities, and earthquakes, with a particular interest toward the phase unwrapping problems.

Dr. Pepe was a recipient of the 2014 Best Reviewer mention of the IEEE Geoscience and Remote Sensing Letters and the 2017 Best Reviewer mention of the MDPI Remote Sensing journal. He is a reviewer for several peer-reviewed international journals.

Giovanni Onorato was born in Naples, Italy, in 1980. He received the Laurea degree (*cum laude*) in physics with a specialization in particle physics, and the Ph.D. in experimental and applied physics with the University of Naples "Federico II," Naples, in collaboration with the Istituto Nazionale di Fisica Nulceare, (INFN section) Naples, and the SLAC Laboratory, Stanford University, Palo Alto, CA, USA.

He was with Fermilab, Chicago, IL, USA, for a particle physics experiment where he increased and perfected his skills in data analysis, statistics, and multivariate analysis. After one year of collaboration with the INFN section of Lecce for an experiment who takes place at the PSI Laboratory, Zurich, Switzerland, he became Researcher with IREA-CNR, Naples, in 2014, started working with the optical fiber and laser group.

In 2017, he started working in the microwave remote sensing field, in particular with the InSAR technique for surface deformation time-series generation, where he is nowadays involved. His work has been focused on the data analysis and the optimization of data reconstruction process, in particular on the phase unwrapping problem and the exploitation of distributed computing architectures, with the application of deep learning techniques.

Paolo Berardino was born in Avellino, Italy, in 1971. He received the Laurea degree in nautical sciences from the Naval Institute University, Naples, Italy, in 1998, with thesis on SAR geocoding.

He joined the Istituto per il Rilevamento Elettromagnetico dell'Ambiente (formerly IRECE), Institute of the Italian National Research Council, Naples, in 1999, where he is currently a Researcher. He is interested in the development of algorithms geocoding of synthetic aperture radar (SAR) images and studies of surface deformation by using differential SAR interferometry. He has collaborated in the development of a new approach for the analysis of the temporal evolution of the deformation of the earth's surface based on the combination of differential interferograms [Small BAseline Subset (SBAS) technique]. Over the years, he has participated actively in the upgrading of technical SBAS (high resolution, geometric registration, data integration ERS/ENVISAT, GIS integration). He has participated in several studies of volcanic areas (Etna, Campi Flegrei, Vesuvius, Tenerife), seismogenic (central Apennines, Greece), landslide areas (Maratea) and urban areas (Naples, Los Angeles) using the technique SBAS and collaborating with different national scientific institutions (Vesuvius Observatory, INGV, IRPI) and international (JPL, UCM).

His work is currently focused on the development of airborne SAR interferometry technique, in partilucar on algorithms for elaboration of data acquired from no linear flight tracks.

Prospero De Martino was born in Naples, Italy, in 1970. He received the Laurea degree in geological sciences from the University of Naples Federico II, Naples, Italy, in 1995.

From 1996 to 1998, he was a Research Assistant at the Department of Geophysics and Volcanology, University of Naples Federico II. Since 1998, he has been with the Osservatorio Vesuviano, Istituto Nazionale di Geofisica e Vulcanologia, Naples, where he is currently a Researcher. His research interests include geodetic monitoring of active volcanoes, high precision GPS data processing and analysis, development of GPS-based deformation monitoring systems, integration of GPS and classical geodetic data with Interferometric synthetic aperture radar techniques, volcanic hazards, and risk assessment.

Riccardo Lanari (M'91–SM'01–F'13) received the Laurea degree in electronic engineering (*summa cum laude*) from the University of Naples, Federico II, Naples, Italy, in 1989.

In 1989, he joined IRECE and after that IREA, both Research Institutes of the Italian Council of Research (CNR), Naples. He has 30 years of research experience in the remote sensing field, particularly on space-borne synthetic aperture radar (SAR) and SAR interferometry data processing methods developments, and their applications in the geosciences. He was a Visiting Scientist in different foreign research institutes, including the German Aerospace Research Establishment (DLR), Oberphaffenhofen, Germany, in 1991 and 1994, the Institute of Space and Astronautical Science, Kanagawa, Japan, in 1993, and the Jet Propulsion Laboratory, Pasadena, CA, USA, in 1997, 2004, and 2008. He has been an Adjunct Professor of electrical communication with the University of Sannio, Benevento, Italy, from 2000 to 2003 and, from 2000 to 2008, a main Lecturer with the Institute of Geomatics, Barcelona, Spain. Moreover, he has achieved the national scientific habilitation as a Full Professor of telecommunications in 2013 and as a Full Professor of geophysics in 2014. Since 2011, he has been the Director of the IREA-CNR. He has coauthored the book *Synthetic Aperture Radar Processing* (CRC Press, 1999) and 117 peer-reviewed publications on ISI journals that have, nowadays, more than 10000 citations. He holds two patents.

Dr. Lanari has been a member of the Advisory Board of the Italian Space Agency for the COSMO-SkyMed missions of first and second generation since 2015 and of the National Commission for the Prevision and Prevention of Big Risks (*Commissione Nazionale Grandi Rischi*) since 2017. He received from NASA a recognition in 1999 and a group award in 2001 for his activities related to the SRTM mission. He received the Dorso prize in 2015, for the Special Section "Research," an association held under the patronage of the Senate of the Italian Republic. Moreover, he received the Christiaan Huygens Medal in 2017 of the European Geosciences Union. He has been a Distinguished Speaker of the Geoscience and Remote Sensing Society of the IEEE since 2001 and he has lectured in several national and foreign universities and research centers and served as a Chairman/Convener and/or Scientific Program Committee Member at many international conferences.